On morphology and amplitude of 2D and 3D thermal anomalies induced by buoyancy-driven flow within and around fault zones

Laurent Guillou-Frottier[1,2], Hugo Duwiquet[1,2,3], Gaëtan Launay[4], Audrey Taillefer[5], Vincent Roche[6], Gaétan Link[7].

[1]BRGM, Georesources Division, 45060, Orléans, France
[2]ISTO, UMR7327, Université d'Orléans, CNRS, BRGM, 45071 Orléans, France
[3]TLS-Geothermics, 31200, Toulouse, France
[4]Laurentian University, P3E2C6, Sudbury, Canada
[5]CFG Services, 45060, Orléans, France
[6]ISTEP, UMR7193, Sorbonne Université, CNRS-INSU, 75005, Paris, France
[7]GET, UMR 5563, Université Toulouse III-Paul Sabatier, CNRS, IRD, CNES, 31400, Toulouse, France

Correspondence to: Laurent Guillou-Frottier (l.guillou-frottier@brgm.fr)

Abstract.

In the first kilometres of the subsurface, temperature anomalies due to heat conduction processes rarely exceed 20-30 °C. When fault zones are sufficiently permeable, fluid flow may lead to thermal anomalies much higher, as evidenced by the emergence of thermal springs or by fault-related geothermal reservoirs. Hydrothermal convection triggered by buoyancy effects creates thermal anomalies whose morphology and amplitude are not well known, especially when depth- and time-dependent permeability are considered. Exploitation of shallow thermal anomalies for heat and power production partly depends on the volume and on the temperature of the hydrothermal reservoir. This study presents a non-exhaustive numerical investigation of fluid flow models within and around simplified fault zones, where realistic fluid and rock properties are accounted for, as well as appropriate boundary conditions. 2D simplified models point out relevant physical mechanisms for geological problems, such as "thermal inheritance" or splitting plumes showing a pulsating behaviour. When permeability is increased, the classic "finger-like" upwellings evolve towards a "bulb-like" geometry, resulting in a large volume of hot fluid at shallow depth. In the simplified 3D models, where fault zone dip angle and fault zone thickness are varied, the anomalously hot reservoir exhibits a kilometre-sized "hot air balloon" morphology, or, when permeability is depth-dependent, a "funnel-shape" geometry. For thick faults, the number of thermal anomalies increases but not the amplitude. The largest amplitude (up to 80-90°C) is obtained for vertical fault zones. At the top of a vertical, 100 m wide, fault zone, temperature anomalies greater than 30°C may extend laterally over more than 1 km from the fault boundary. These preliminary results should motivate further geothermal investigations of more elaborated models where topography and fault intersections would be accounted for.

1. Introduction

In the shallow crust, several geological systems meet the necessary conditions for the occurrence of fluid circulation.
35 Tectonically active systems, ash-flow calderas, sedimentary basins and especially crustal fault zones correspond to dynamic systems which are sufficiently porous and permeable to host fluid circulation (e.g. Simms and Garven, 2004; Hutnak et al., 2009; Lopez et al., 2016; Patterson et al., 2018a ; Duwiquet et al., 2019). As soon as rock permeability is large enough, meteoric, metamorphic or magmatic fluids can flow along kilometer-scale pathways, at velocities reaching up to several meters per year (e.g. Forster and Smith, 1989 ; Lopez and Smith, 1995). When fluid velocity is sufficiently large, heat can be advected
40 with the fluid to shallow crustal levels (e.g. Ague, 2014), leading to the settlement of hydrothermal reservoirs and thus to exploitable thermal anomalies. Similarly, when cold fluid is transferred to deep levels (or when deep hot fluids rise in the intermediate crust), precipitation of minerals can be favored and mineralizing processes may form exploitable ore deposits (e.g. Fehn et al., 1978 ; Boiron et al., 2003 ; Weis et al., 2012). Whether geothermal resources or mineral resources are targeted, the main questions that have generally to be solved deal with the location and with the volume of the reservoir. This study is
45 focused on the « geothermal side » of hydrothermal resources (i.e. mineralizing processes are not considered) and particularly on the formation of anomalously hot and shallow hydrothermal reservoirs.

In shallow permeable zones, at the scale of kilometer-sized reservoirs, two main processes can control fluid circulation: (i) significant pressure gradients, which can result from an important topography or from magmatic or metamorphic fluid
50 production, and (ii) buoyancy effects, due to temperature-dependent fluid density, that can result in thermal convection in permeable media. In the first case, the term « forced convection » is employed while in the second case, « free convection » is used. Although both processes can occur at the same time (see for example the numerical models of the Basin and Range extensional geothermal systems, by McKenna and Blackwell, 2000), one of the two convection modes may predominate. For example, in the case of an important topography (1000 − 2000 m), forced convection may control the fluid flow regime as in
55 the case of Alpine hydrothermal systems (e.g. Sonney and Vuataz, 2009). However, in the case of a fault zone with a high permeability, free (thermal) convection may prevail over forced convection.

The possibility for thermal convection to occur within a permeable medium was often tested with the calculation of the Rayleigh number (e.g Turcotte and Schubert, 2002). This dimensionless number depends on the imposed temperature gradient,
60 on the considered geometry and on fluid and rock properties. If the Rayleigh number exceeds a critical value, then thermal convection occurs. The critical value of $4\pi^2$ (Lapwood, 1948) was determined by linear stability analysis for an infinitely long homogeneous porous medium, where fixed temperature conditions are applied on both horizontal boundaries, and for a constant viscosity fluid. For different (and more realistic) boundary conditions (e.g. fixed heat flow at depth and fixed pressure at the surface) the critical Rayleigh number is decreased (see Jaupart and Mareschal, 2011). When temperature-dependent
65 viscosity is accounted for, Lin et al. (2003) demonstrated that the critical Rayleigh number is also decreased when compared

to the constant viscosity case. In other words, when realistic boundary conditions are considered and when appropriate fluid properties are taken into account, the critical permeability for which free convection would occur is not as high as previously thought.

70   In the case of a finite size vertical fault zone, Malkovski and Magri (2016) developed a new linear stability analysis accounting for temperature-dependent fluid viscosity. They showed, in accordance with Wang et al. (1987), that the critical Rayleigh number can be expressed with the fault aspect ratio (half-width over depth), but also with a dimensionless thermal parameter describing the temperature-dependence of the fluid viscosity. One of their conclusions is that the Rayleigh theory may not be sufficient when fluid properties are adequately considered. In addition, the critical permeability for which free convection

75   develops may be four times lower than initially predicted within the constant viscosity hypothesis. One limit of their theoretical study lies however in the investigated temperature range, limited to a domain where a linear fit to density variation holds. Indeed, for temperatures greater than 300°C, the linear fit does not hold anymore, and one must thus refer to a numerical approach where an appropriate density law (non-linear, pressure- and temperature-dependent) can be accounted for.

80   In this study, we focus on hydrothermal convection that could lead to the establishment of exploitable thermal anomalies. Geothermal resources leading to power production generally require temperatures higher than 150°C, and present-day exploration projects tend to target supercritical conditions, involving much higher temperatures (« high enthalpy geothermal systems » or, as recently suggested, « superhot geothermal systems » ; e.g. Scott et al., 2015; Watanabe et al., 2019), in particular around the brittle-ductile transition (350-400°C, Violay et al., 2017). It is thus necessary to study hydrothermal

85   convection where temperature can exceed 300°C, a domain for which fluid properties are highly nonlinear. For example, Jupp and Schultz (2000) demonstrated that the surprising constant temperature of black smokers (around 380°C) could be explained by the maximization of the « fluxibility » parameter, which depends on thermodynamic properties of water (density, viscosity and specific enthalpy).

90   Besides accounting for appropriate fluid properties, studies on hydrothermal convection need to consider realistic rock permeability. This physical property, initially supposed to be « static », has been more and more considered as « dynamic », not only through field and petrologic observations (e.g. Jamtveit et al., 2009 ; Faulkner et al., 2010 ; Stober and Bucher, 2015) but also in numerical models and laboratory experiments (Tenthorey and Cox, 2003; Tenthorey and Fitzgerald, 2006; Coelho et al., 2015; Ingebritsen and Gleeson, 2015 ; Mezri et al., 2015 ; Weis, 2015 ; Launay et al., 2019). Several mechanisms can

95   explain spatial (e.g. depth-dependent) and temporal (e.g. stress-dependent) variations of permeability. For example, fluid-rock interactions may involve mineralogical transformations leading to continuous increase of permeability (Launay, 2018). A gradual permeability increase in a fault damage zone has been suggested by Louis et al (2019) to explain temporal evolution of the Beowawe hydrothermal system in Nevada. However, depending on the hydrogeologic and tectonic setting, sudden increase or decrease of permeability could also happen and should significantly affect the fluid flow conditions. If the effect

100   of heterogeneous and dynamic permeability has already been studied around magmatic intrusions (e.g. Gerdes et al., 1998 ; Weis et al., 2012 ; Scott and Driesner, 2018 ; Launay, 2018), this is not the case for fault zones.

This study is intended to show, with a numerical modeling approach, how hydrothermal convection establishes in a permeable fault zone, how convective patterns are organized, and which kind of particular phenomena can be observed. The effects of

105   topography are not accounted for in this preliminary approach. First, 2D numerical models are presented, with constant, depth-dependent and time-dependent permeability. The effects of a~variable permeability are discussed in terms of convective patterns and temperature distribution (morphology and amplitudes of thermal anomalies). Finally, simple 3D numerical models of hydrothermal convection in permeable fault zones illustrate how positive thermal anomalies can establish at shallow depths, thereby~illustrating an interesting predictive tool for geothermal exploration, where maps of temperature anomalies often

110   correspond to the first major information~(e.g. Clauser and Villinger, 1990 ; Bonté et al., 2010 ; Garibaldi et al., 2010 ; Guillou-Frottier et al., 2013).

2. Typical structural settings and permeability values for hydrothermal systems

Apart from geothermal systems associated with a magmatic heat source which drives excess heat toward shallow depths, fault zones may serve as efficient conduits for deep hot fluids to rise up to the surface (e.g. Curewitz and Karson, 1997; Fairley and

115   Hinds, 2004; Person et al., 2012; Bense et al., 2013; Sutherland et al., 2017). Faulds et al. (2010) analyzed different geothermal systems in back-arc domains (Nevada and western Turkey) and concluded that specific structural settings were involved in the localization of geothermal systems. Discrete steps in normal fault zones, terminaisons of major normal faults, or fault stepovers (among other fault features) appear to control locations of the investigated geothermal systems. On the basis of field studies in western Turkey, Roche et al. (2019) suggested that the intersection between crustal-scale low-angle normal faults and

120   transfer~faults represents the first-order control on geothermal systems.

Fault stepovers have also been suggested to control the location of supergiant gold deposits (Micklethwaite et al., 2015), which correspond to fossil hydrothermal systems. According to the authors, formation of supergiant gold deposits would be associated to transient variations of permeability, whose value may reach 10^{-12} m². Person et al. (2012) modelled hydrothermal fluid flow

125   at intersections of 10–20 m wide fault zones. They reproduced typical hydrothermal activity of the Basin and Range extensional tectonic province with permeability values between 5 and 7 10^{-13} m². Such high permeability values were also proposed in low-temperature active geothermal systems (e.g. Truth and Consequences geothermal system in New Mexico, Pepin et al., 2015).

130   When larger fault zones are considered, smaller permeability values are inferred. According to recent studies on different geological systems, it seems that permeability greater or around 10^{-14} m² could represent a typical value for which geological

data can be reproduced. For example, in the case of the 300 m wide Têt fault system, French Pyrenees, Taillefer et al. (2018) reproduced locations and temperatures of the 29 thermal springs with a permeability value of 10^{-14} m². In a 3D model of the Lower Yarmouk Gorge, at the border between Israel, Jordan and Syria, Magri et al. (2016) also reproduced clusters of thermal

135   springs with realistic temperatures, with a fault permeability of 2.3 10^{-14} m². Roche et al. (2018) qualitatively reproduced temperature profiles measured within fault-related geothermal systems in western Turkey when permeability of detachments (low-angle normal faults, 200-400 m wide) equals 10^{-14} m². When fault permeability is higher, cold downwellings may be favored within the fault, as in the numerical simulations of the Soultz-sous-Forêts geothermal system where fault width equals 100 m (Guillou-Frottier et al., 2013). In the case of the Pontgibaud crustal fault zone (French Massif Central), Duwiquet et al.

140   (2019) reproduced present-day surface heat flow and temperature gradient for a maximum permeability of 1.6 10^{-14} m², a value for which a high temperature (150°C) hydrothermal reservoir could ~~settle~~ at a depth of 2.5 km. ~~It may be worth to~~ consider the possibility of a critical fault permeability above which positive thermal anomalies disappear in favor of negative anomalies, but Lopez and Smith (1995) ~~already~~ showed that the role of host rock permeability has also to be taken into account (see also Della-Vedova, 2008). ~~In addition,~~ the permeability ratio between fault zone and host rocks may ~~correspond to~~ one critical

145   parameter for building a convective regime diagram, as suggested by Duwiquet et al. (2019). Consequently, the complex coupling between host rock and fault zone permeability will be also considered in this study.

3. Method

All numerical simulations presented in this study correspond to ~~the~~ coupling of the heat equation with ~~the~~ Darcy law, while mass conservation is applied. We used the Comsol Multiphysics™ software, ~~by~~ computing transient evolution of hydrothermal

150   convection lasting in some cases, up to several hundreds of thousands years. In the more elaborated experiments (3D geometry), fluid density is temperature- and pressure-dependent, and fluid viscosity is temperature-dependent. Governing equations are detailed in Guillou-Frottier et al. (2013). Physical ~~law~~ and numerical procedure are detailed in Appendix A. We restrict our study to the (P,T) domain where fluid stays in a ~~fluid~~ phase (i.e. no vapor phase), as for example in the case of pure water at 350°C at 2-3 km depth.

155

Before performing 3D simulations of hydrothermal convection in fault zones, 2D experiments are presented in order to highlight and review how convective patterns are organized in a permeable medium, where permeability is progessively constant, depth-dependent and time-dependent. The first 2D simulations (Fig. 1 to Fig. 7) are based on the same set-up, boundary conditions and physical properties as those used by Rabinowicz et al. (1998). A 1.5 km-thick and 4.5 km-wide

160   permeable medium is thermally insulated on both vertical sides. Fixed temperature conditions of 0°C and 400°C are imposed on top and bottom boundaries, respectively. A no flow condition is imposed on all boundaries except on the top one, where a fixed pressure of 10^5 Pa is present (Fig. 1a).

The second series of numerical experiments deal with 3D models of hydrothermal convection in a fault zone embedded in low

165   permeable host rocks. Benchmark tests are performed in order to reproduce the already published results by Magri et al. (2017). For these particular 3D benchmark tests (detailed in Appendix B), a simplified density law (linear decrease with temperature) is imposed by the Magri et al. (2017) study. In the other 3D simulations (Fig. 8 to Fig. 14), a more realistic pressure- and temperature-dependence for fluid density is used, and a more realistic thermal boundary condition is applied at the bottom boundary (a fixed heat flow condition). One of the objectives of these 3D models is to understand how and where thermal

170   anomalies develop. The role of the dip angle of the fault zone is tested, as well as the role of permeability distribution within the model.

4. Results from 2D models

4.1 Constant permeability

Figure 1 illustrates hydrothermal convection for constant permeability values, from the onset of thermal convection (Fig. 1b)

175   to vigorous convection, just before unsteady or turbulent convective patterns dominate. As already shown by many studies (e.g. Rabinowicz et al., 1998) the vigor of thermal convection (or the number of upwellings, or the maximum fluid velocity value) increases with a permeability increase. Convective wavelength decreases with a permeability increase, and up to 8 internal upwellings (i.e. without considering the half plumes at lateral boundaries) are obtained in the most permeable case (10^{-13} m², Figure 1i). While changes in the convective patterns are understandable (the more permeable is the medium, the

180   more active is the convective regime), the evolution of thermal characteristics is less obvious. The right column in Fig. 1 shows horizontal temperature profiles at mid-depth, with numerical values of the horizontally-averaged temperature $< T >$ and of the temperature excess ΔT compared to this average. It must be noted that due to asymetric flow conditions at horizontal boundaries and non-linear fluid properties, the averaged temperature at mid-depth exceeds 200°C, the temperature that would be present in the purely conductive case with no heat source. When thermal convection occurs, this horizontally-averaged

185   value of 200°C can be obtained at mid-depth if fluid density varies linearly with temperature and when a no flow condition – as at bottom boundary – is imposed on the top surface.

Finally, Fig. 1 shows that while permeability increases, the increase of the horizontally averaged value $< T >$ is not regular, as well as the temperature excess ΔT. Similarly, the minimum and maximum temperatures reached at mid-depths (values in

190   brackets below horizontal temperature profiles) do not evolve regularly from top to bottom experiments. The obtained convective patterns in Fig. 1 will be named in the following as « finger-like » upwellings as in, e.g., Zhao et al (2003), with almost vertical isotherms bounding upwellings and downwellings, as also illustrated by Rabinowicz et al. (1998).
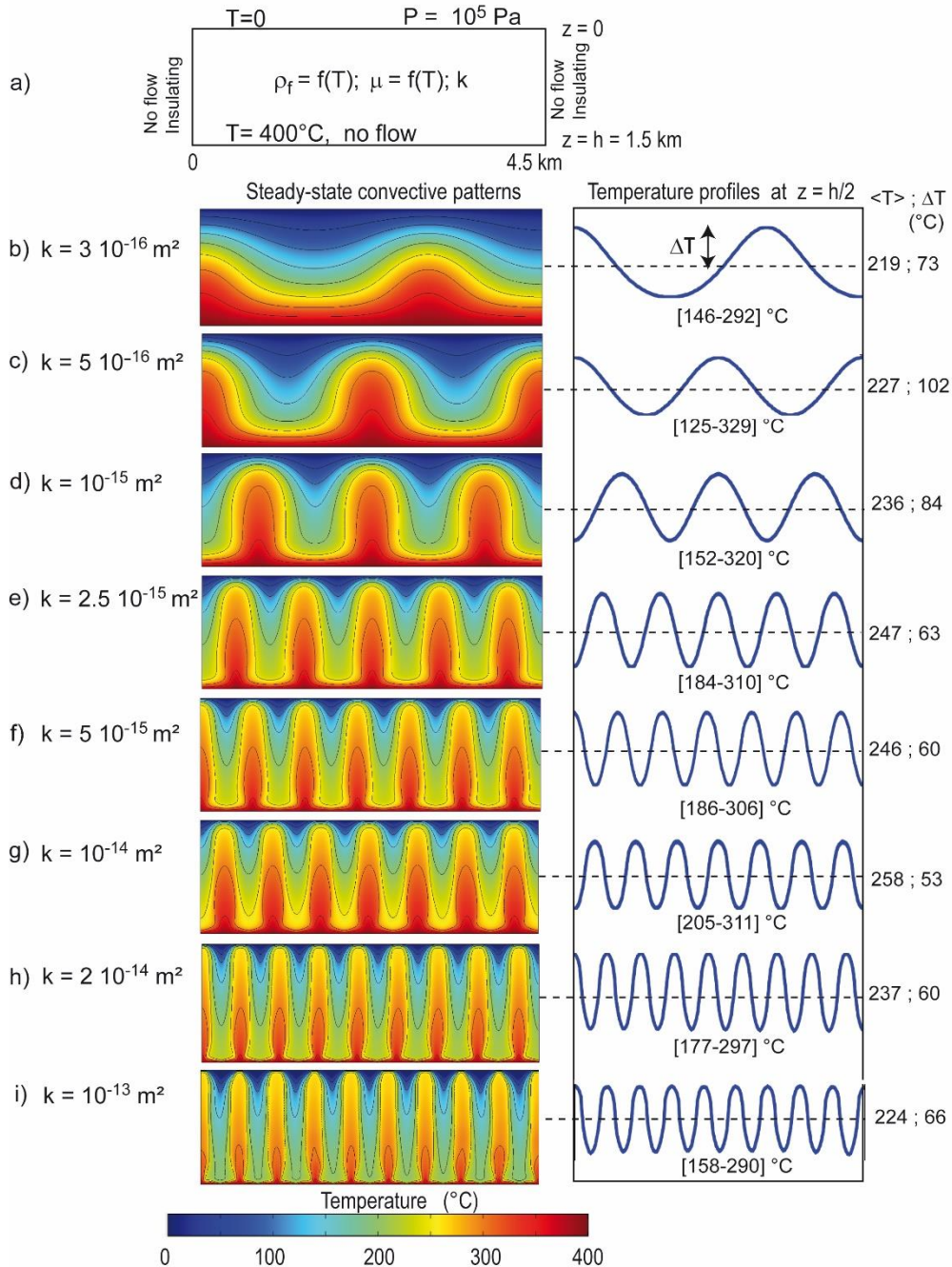
Figure 1: Steady-state temperature fields obtained for different values of the medium permeability. Left column shows temperature
195 **fields and right column illustrates a horizontal temperature profile at mid-depth. Averaged temperature at mid depth (<T>) and**
temperature anomalies (ΔT) are indicated on the right of each profile. Numerical set-up and boundary conditions are illustrated in
a) and detailed in the text. For all experiments, the maximum mesh element size is 20 m. Hydrothermal convection (b) is observed
for permeability around 3 10^{-16} m (a pure conductive regime is obtained for smaller permeability). The number of upwellings
increases with increasing permeability. Above 10^{-13} m², convection exhibits unsteady patterns, including typical Y-shaped and
200 **splitting plumes (see section 4.5).**

4.2 Depth-dependent permeability

In the shallow crust (above the brittle-ductile transition), permeability is ~~supposed~~ to decrease with increasing lithostatic pressure (e.g. Manning and Ingebristen, 1999; Saar and Manga, 2004; Achtziger-Zupančič et al., 2017) but this depth-

205   dependence may be less effective in highly permeable fault zones, like extensional faults in the Larderello and other geothermal systems (Della-Vedova et al., 2008; Scibek, 2020). In the case of a constant pressure boundary condition at the top surface (a realistic condition for geological systems ~~when compared to~~ a "no flow" condition), the fact that permeability decreases with depth has important consequences on convective patterns. In Fig. 1, the finger-like upwellings are embedded within their cold counterparts (finger-like downwellings), thus exhibiting a perfect geometrical symmetry. ~~On the opposite,~~ when permeability

210   decreases with depth, the number of upwellings decreases (Fig. 2). Case A corresponds to Fig. 1f, and cases B, C and D illustrate experiments with an exponentially-decreasing permeability with depth. The decrease ~~of~~ the number of upwellings can be explained by the asymmetric distribution of temperature and permeability: cold fluids are located in the most permeable zones, whereas hot fluids at depth encounter less permeable medium. ~~In other words, fluid flow is facilitated in cold zones.~~ Consequently, cold downwellings are favored and a general cooling is obtained in the last case (see mid-depth temperature

215   profiles in Fig. 2). Contrary to the constant permeability cases, individual upwellings do not show a regular distribution of finger-like upwellings since the cooling effect in the upper levels dominates and tends to destroy upwelling heads. According to their geometry, these upwellings will be named « triangular-like » upwellings (see in particular the cases C and D).
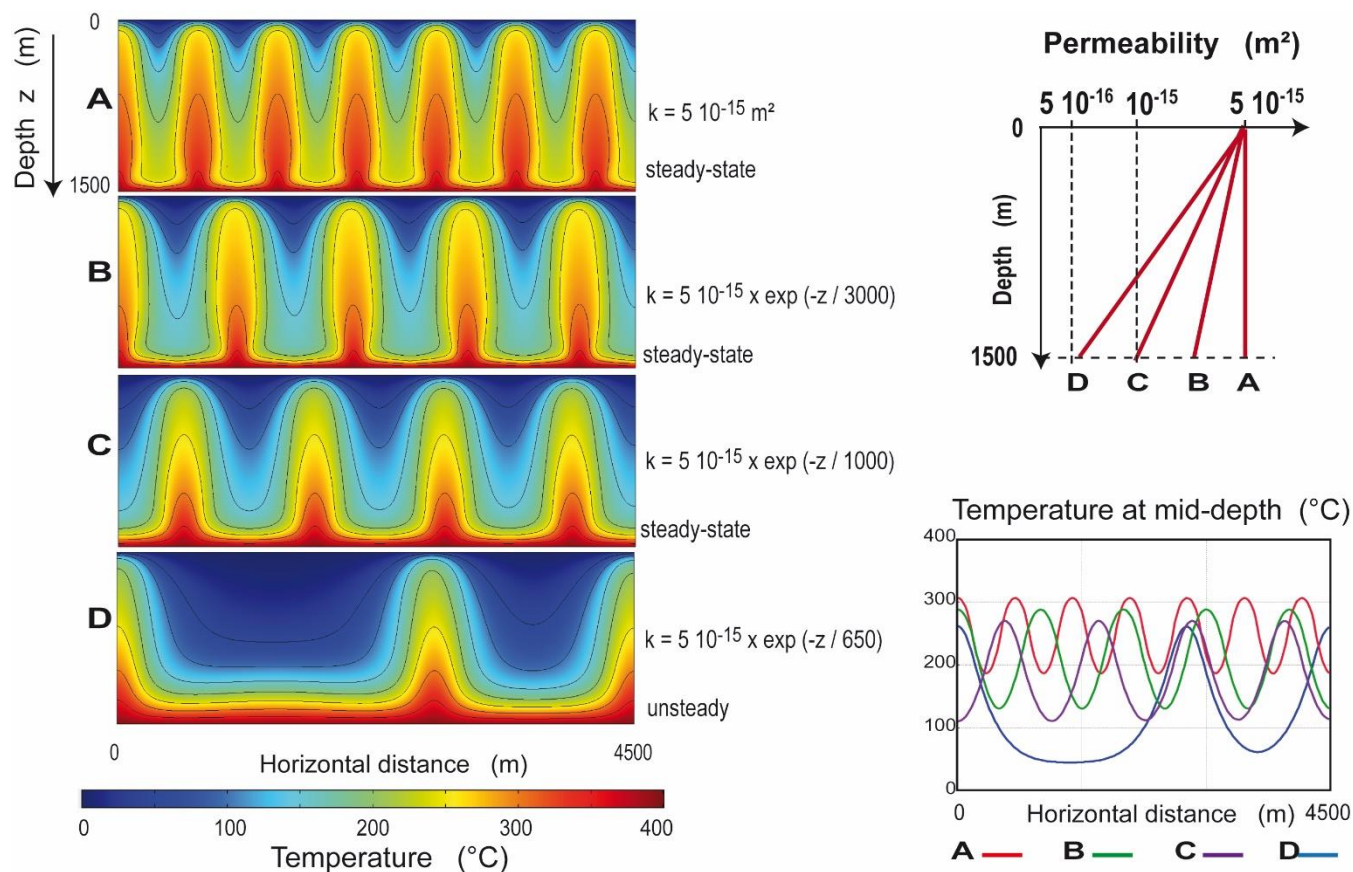
Figure 2. Effect of the depth-dependence (decrease) of the permeability, here taken as exponential. The number of upwellings decreases when the depth-dependence is accounted for: 6 internal upwellings are obtained for the constant permeability case (labelled "A", top pattern) but only one for the ~~important~~ exponential decrease ("D", bottom). Horizontal temperature profiles at mid-depth (bottom right) illustrate the major cooling effect as well as the increasing temperature contrast between upwellings and downwellings when deph-dependence is increased. See text for explanations.

4.3 Time-dependent permeability

4.3.1 From a depth-dependent to a constant permeability: instantaneous increase

Seismic activity could reactivate former deformation zones and thus ~~trigger~~ instantaneously a permeability increase (e.g. Sibson, 1992; Cox, 2010). Figure 3 illustrates the modifications of temperature patterns when a sudden increase in permeability is applied to ~~the previous~~ case C of Fig. 2. The depth-dependence of permeability is instantaneously cancelled and a constant permeability of $5\ 10^{-15}$ m² is applied. Because permeability is increased at the bottom of the system, deep hot fluids can move upward more easily, and the triangular-like upwellings evolve toward a « bulb-like » geometry, with a shrinking tail and a large head. Surprisingly, the convective pattern illustrated in Fig. 1f (permeability of $5\ 10^{-15}$ m²) – i.e. with finger-like

upwellings – is not recovered although permeability is the same. ~~Actually, the initial thermal regime in the first case (Fig. 1f)~~ ~~corresponds to a conductive regime whereas in Fig. 3, the initial regime corresponds to the triangular-like geometry. Similar~~

235 ~~observations are described in section 4.4.~~

~~Another interesting feature deals with the thermal anomalies that are generated by those bulb-like upwellings.~~ Figure 3 shows that the instantaneous increase in permeability has a warming effect at a depth of 600 m and a cooling effect at a depth of 1300m. The warming effect corresponds to the larger head, and the cooling effect to the shrinking tail. When compared to the

240 case of triangular-like upwellings, temperature differences reach, +50°C and -70°C, respectively (bottom plots of Fig. 3).
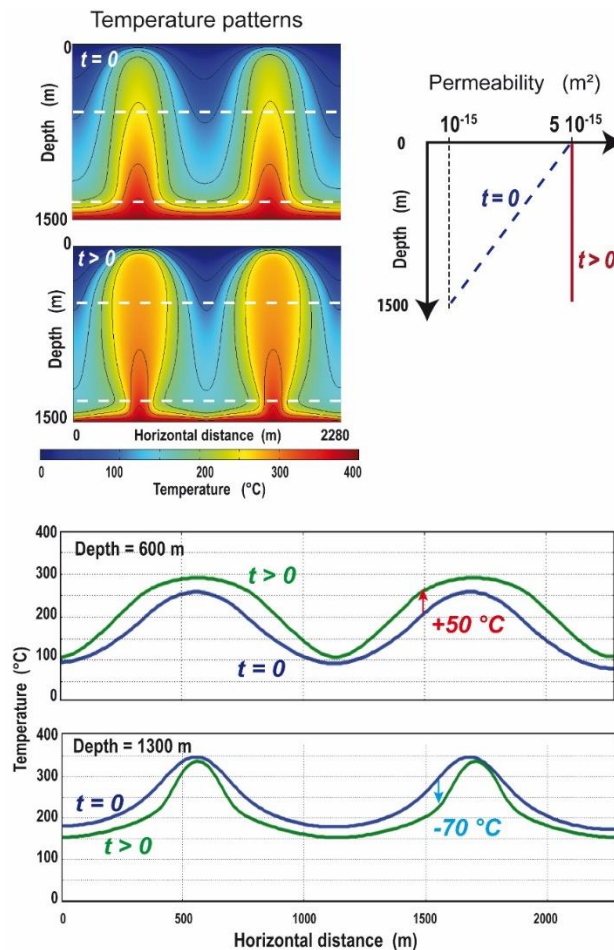
Figure 3. Effet of a sudden increase of permeabilty: from a depth-dependent variation (dashed line in the top-righ plot) to a higher constant permeability (red line). Temperature patterns (top left) show that the initial « triangular-like » geometry (t=0) of the upwellings evolves toward a « bulb-like » geometry. Lower plots show the temperature variations along the white dashed lines

245 **illustrated in the temperature patterns. Bulb-like regime involves higher positive temperature anomalies in the upper part of the system (up to 50°C), and higher negative temperature anomalies in the lower part (down to -70°C).**

4.3.2 From a constant to a higher permeability: time-dependent increase

250 ~~Contrary to an instantaneous increase, a~~ progressive increase of permeability could be related to fluid-rock interactions that ~~could~~ trigger the dissolution of ~~some~~ minerals like quartz and calcite. This dissolution induces porosity generation which in turn increases permeability (Scott and Driesner, 2018; Launay et al., 2019). One could also invoke tectonic processes like regional uplift which modifies pressure conditions that partly control permeability. ~~On the opposite,~~ progressive mineral deposition in the permeable structure can ~~seal the deformation zone,~~ result~~ing~~ in a permeability decrease (e.g. Lowell et al., 1993). Figure 4 illustrates the effects of a non-instantaneous increase of permeability for an initial convective pattern

255 corresponding to a finger-like geometry (constant permeability of 10^{-15} m², case of Fig. 1d). Here, a permeability increase by a factor 20 is imposed over a total duration lasting 20 kyr (see top plot in Fig. 4). This arbitrarily chosen duration allows identif~~ying~~ a transient unexpected warming event, which occurs in the first 10 kyr, ~~in accordance~~ with seismically-induced fault permeability changes described by Howald et al. (2015).
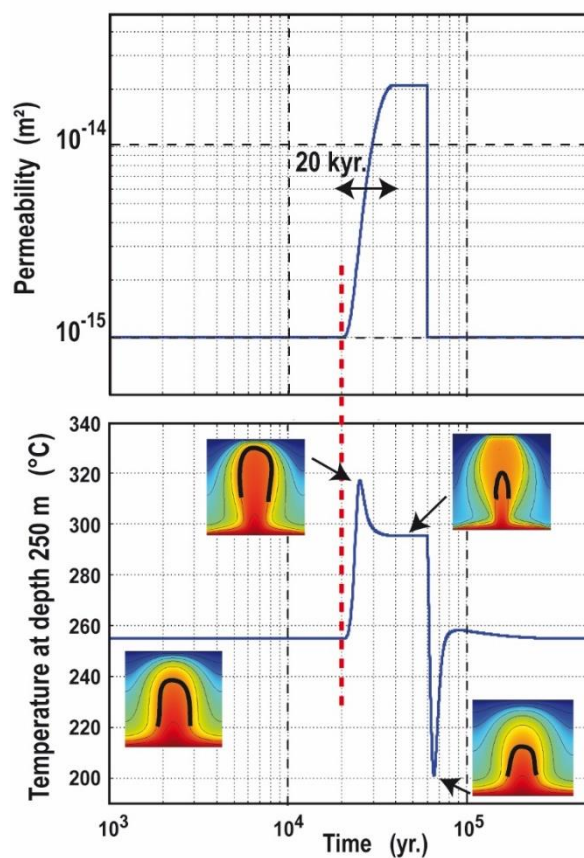
260 **Figure 4. Effect of a time-dependent permeability, increasing by a factor of 20 in 20 kyr. The finger-like geometry (lower left pattern) evolves towards a bulb-like geometry (upper right pattern). Temperature profile (bottom plot) shows short-duration heating and cooling events. The thick black contour on convective patterns corresponds to the 300°C isotherm. . Color-bar (not shown) is the same as in previous figures.**

265 ~~Indeed, w~~hen permeability increases, hot fluid moves upward more easily, thus creating a warming effect at shallow depth, from t = 2.0 10^4 yr. to 2.5 10^4 yr. (see temperature evolution at a depth of 250 m, in the bottom plot). As illustrated by colored patterns in Fig. 4, this first phase corresponds to the transition from a finger-like to a bulb-like pattern. After 2.5 10^4 yr., while permeability is still increasing, a cooling effect dominates, as illustrated by temperature plot and colored patterns, where the thick black line indicates the 300°C isotherm. When permeability is stabilized at 2 10^{-14} m², temperature becomes stable and

270 the bulb-like pattern does not evolve. At time t = 6 10^4 yr., ~~the~~ instantaneous decrease of the permeability toward the initial value of 10^{-15} m² shifts the bulb-like geometry to the expected finger-like geometry. However, ~~it is interesting to note that~~ a short-duration important cooling stage (from 295°C to 200°C) occurs during the instantaneous permeability decrease, before the initial finger-like pattern is recovered.

4.4 Role of initial thermal regime: thermal inheritance

275 As illustrated by Fig. 1f and 3, different steady-state convective patterns can be obtained if initial thermal regime differs: in the case of an initial pure conductive regime, a finger-like geometry is obtained with a permeability of 5 10^{-15} m² (Fig. 1f), while a bulb-like geometry is obtained when the initial thermal regime corresponds to triangular-~~like~~ upwellings (Fig. 3). In the following, different initial thermal regimes are considered and the evolving convective patterns are recorded when permeability is instantaneously increased up to a given value, identical for all cases. This type of simulations can illustrate

280 what could happen in active and polyphased geological systems like orogenic belts.

In Fig. 5, initial permeability (hereafter noted k_0, patterns in the left column) is instantaneously increased to 5 10^{-15} m². The first experiment in Fig. 5 corresponds to Fig. 1f: starting from a conductive regime (flat isotherms), a finger-like geometry is obtained, with 6 internal upwellings. When the initial thermal regime corresponds to a convective pattern obtained with a

285 permeability of 5 10^{-16} m², the finger-like upwellings evolve toward a bulb-like geometry (intermediate and final stages), and the number of internal upwellings slightly increases, from 1 (initial and intermediate stages) to 3 (final steady-state). In the last experiment of Fig. 5, the 3 initial upwellings are conserved, and here again, a bulb-like geometry is promoted. Conservation of the initial number of upwellings will be refered ~~in the following~~ to as « thermal inheritance ». ~~In that later case, the final pattern appears to be unstable, with no half upwellings on the sides, as in the previous case. This is probably due to the fact~~

290 ~~that the box length is not adapted with only 3 upwellings (see Börsing et al., 2017 for discussions on stable convective patterns versus box lengths).~~
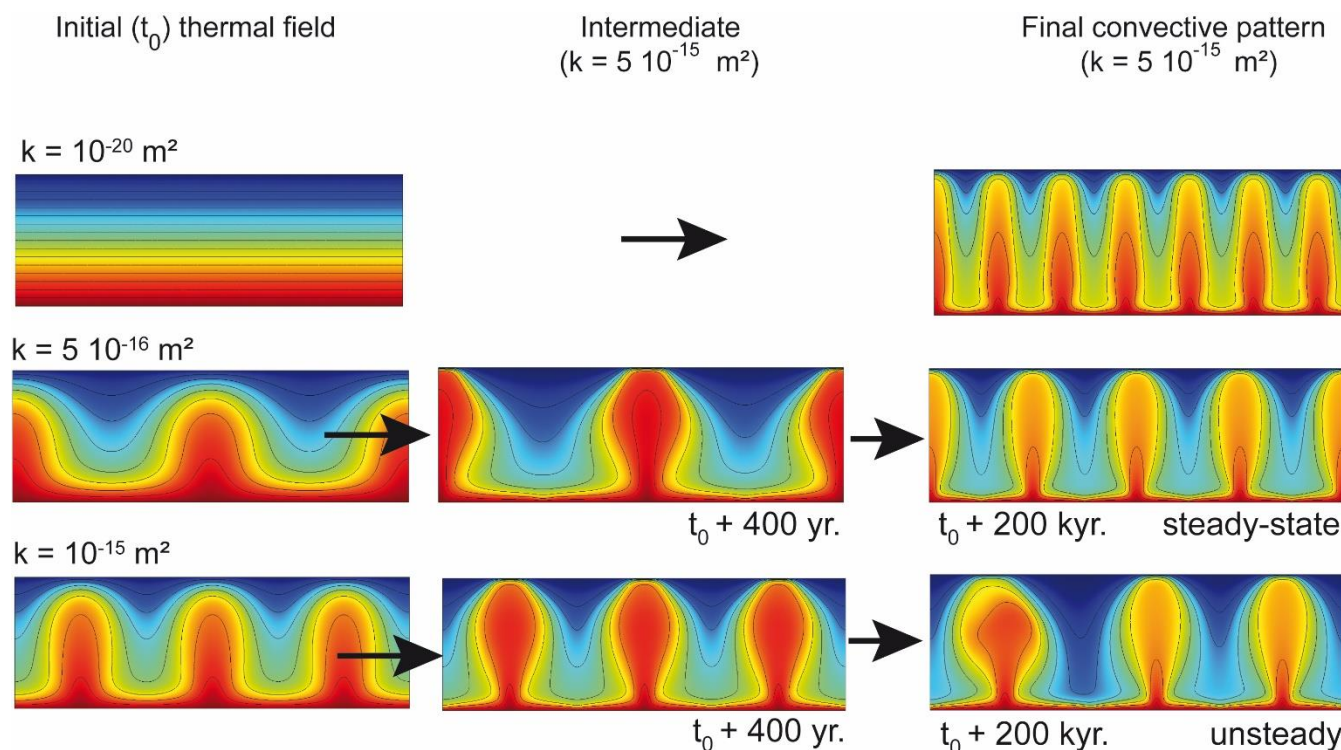
Figure 5. Illustration of "thermal inheritance". For the three cases, the final permeability is the same but initial thermal regime differs ~~from one case to the other~~. In the first case (top row), ~~there is no thermal forcing since~~ the initial thermal regime is purely conductive (top left). A finger-like morphology is obtained for the upwellings. In the two other cases, the convective pattern appears to be controlled or influenced by the initial one. A bulb-like morphology is promoted for the upwellings. Color-bar (not shown) is the same as in previous figures.

Figure 6 shows similar experiments for different box lengths (5, 7 and 10 km): an instantaneous increase of the initial permeability k_0 is imposed. For each experiment, from (a) to (h), initial thermal regime is on the top and the final pattern is below. Fig. 6a corresponds to conditions of Fig. 1f, but box length has been slightly increased (5 km instead of 4.5 km). It follows that 7 internal finger-like upwellings are obtained (and not 6 as in Fig. 1f). For the same box length, the two other experiments (Fig. 6b and 6c) illustrate ~~the same phenomenon as previously described~~ (thermal inheritance): 3 internal upwellings are conserved in Fig. 6b and 4 upwellings in Fig. 6c. As in Fig. 3, the instantaneous permeability increase results in ~~the~~ shrinking of the upwelling tail (see white arrows), thus promoting bulb-like geometries. Without detailing the other experiments for box lengths of 7 and 10 km (Fig. 6d to 6h), it can be easily seen that thermal inheritance is a rule. For each case, the final convective pattern appears to be controlled by the initial one (same number of upwellings).

Instantaneous increase of permeability: from k_0 to $5 \cdot 10^{-15}$ m²

L = 5 km   a) $k_0 = 10^{-16}$ m²   b) $k_0 = 5 \cdot 10^{-16}$ m²   c) $k_0 = 10^{-15}$ m²

L = 7 km   d) $k_0 = 10^{-16}$ m²   e) $k_0 = 5 \cdot 10^{-16}$ m²   f) $k_0 = 10^{-15}$ m²

L = 10 km   g) $k_0 = 10^{-16}$ m²   h) $k_0 = 10^{-15}$ m²
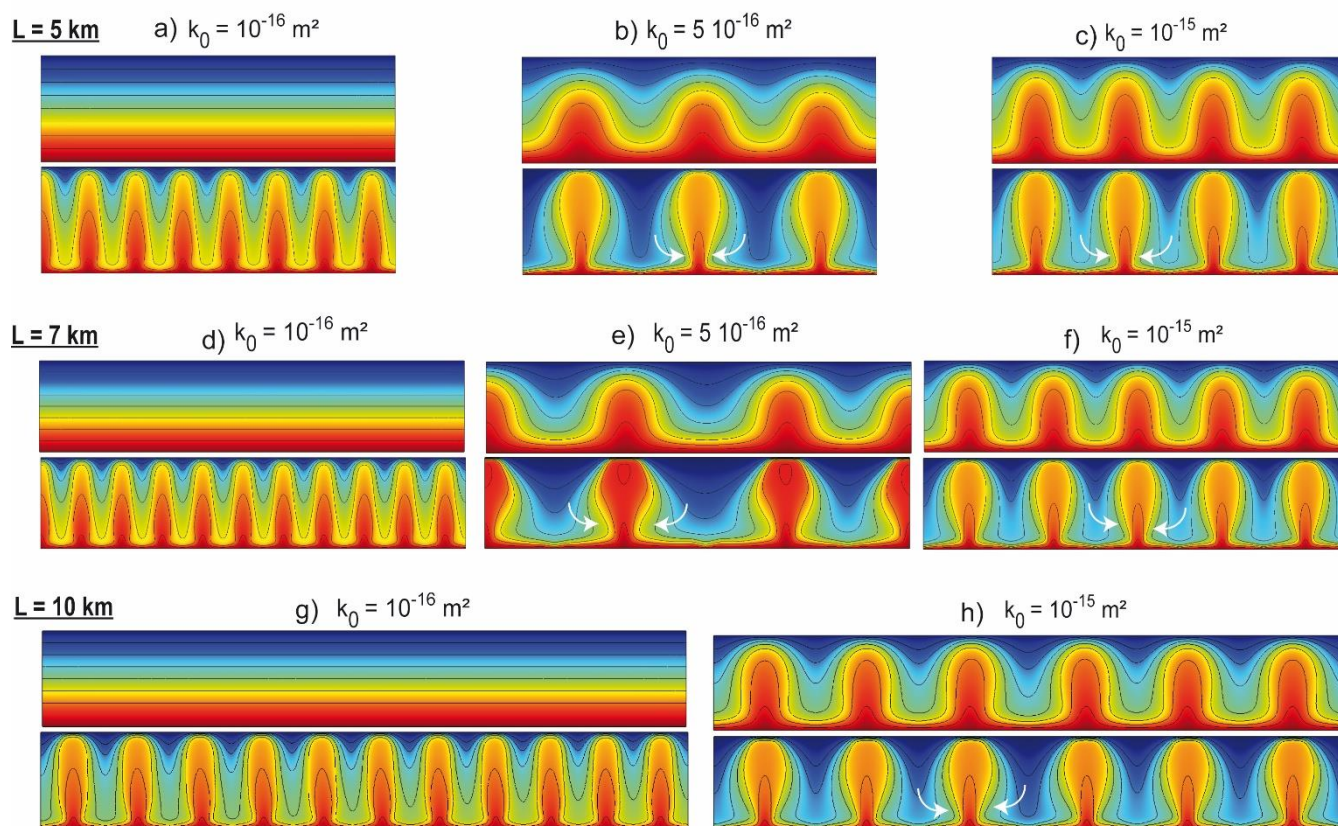
Figure 6. Additional experiments illustrating thermal inheritance for 3 distinct box lengths L. Initial ($t = t_0$) thermal regimes correspond to the figures on the top, obtained with the permeability k_0. At $t > t_0$, for the 8 experiments, permeability is instantaneously increased from k_0 to $5 \cdot 10^{-15}$ m², and the obtained regime after a few hundreds of years is shown at bottom of each experiment. For each box length, the initial thermal regime can represent a conductive regime (cases a, d and g) or a slightly convective regimes (b, e) or a more vigorous convective regimes (c, f and h). For each case, the obtained convective pattern is strongly controlled by the initial one, i.e., the location of upwellings is dictated by that of the previous ones. Note that the finger-like shape of upwellings (a, d and g) is changed to a bulb-like shape with a shrinking base (white arrows) when initial thermal regime is not conductive. Color-bar (not shown) is the same as in previous figures.

4.5 Case of high permeability: splitting plumes

When permeability suddenly increases (Fig. 3 to 5), the bulb-like geometry is favored because hot buoyant fluid has less resistance to ~~flow~~ upward, and fluid velocity increases. In the case of a high permeability involving fluid velocity greater than ~ 10^{-7} m.s^{-1}, the velocity increase ~~involves the~~ separation ~~of~~ the plume head from its tail, as already observed by Coumou et al. (2006). Figure 7 illustrates such a case, where initial permeability (depth-dependent permeability with a maximum value of 10^{-14} m²) is increased to a constant value of $2 \cdot 10^{-14}$ m² (Fig. 7a). The initial convective pattern (triangular-like geometry) evolves promptly toward a bulb-like geometry and a pulsating behavior is observed, exhibiting several splitting stages of the

325 hot upwelling. Even if this convective regime is ~~probably~~ close to a chaotic behaviour, one ~~could however~~ define a time period

of 240–250 yr: similar patterns are observed at time t_0 + 50 yr and t_0 + 300 yr, or at time t_0+ 160 yr and t_0 + 400 yr.
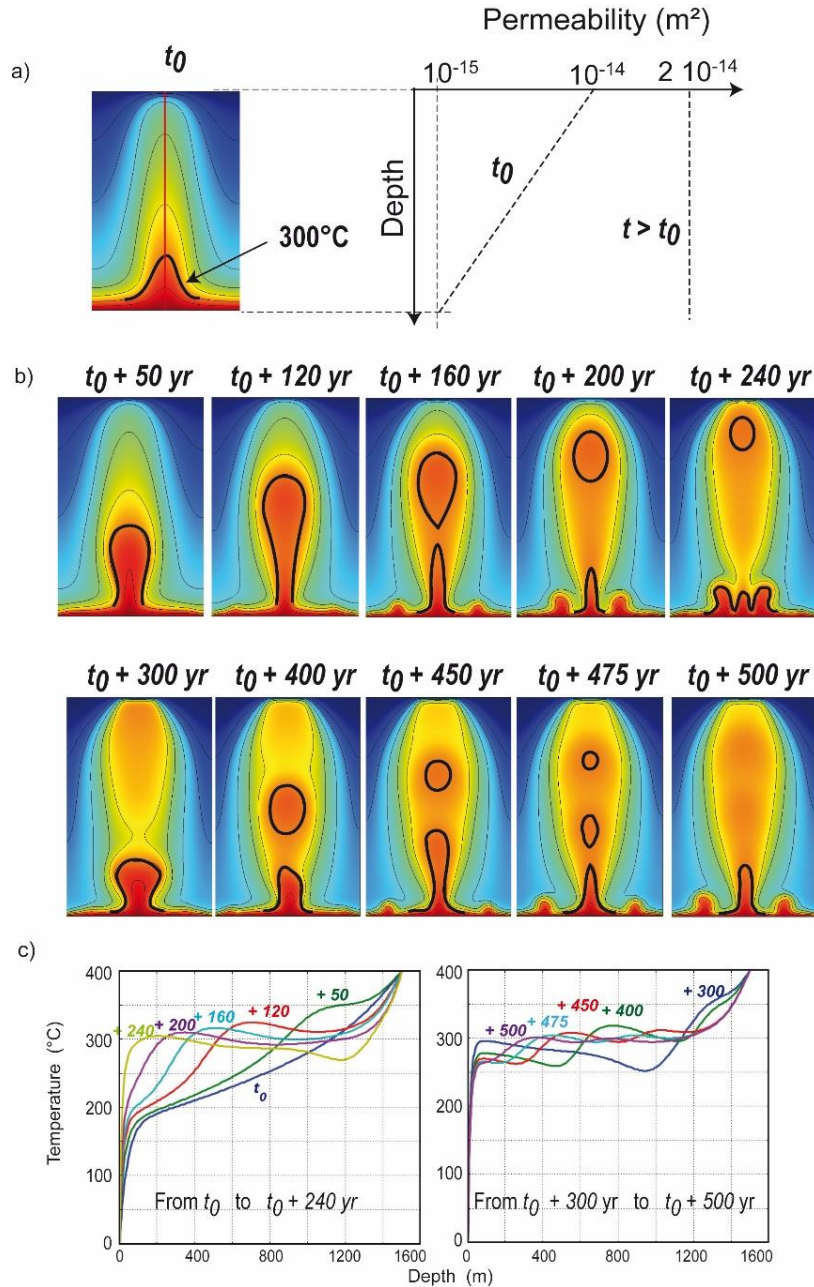
Figure 7. Instantaneous increase of the medium permeability (from 10^{-14} exp(-z/650) at $t = t_0$, to 2 10^{-14} m², at $t > t_0$) resulting in a high velocity upwelling, where the central blob does not lose much energy during ascent. a) steady-state triangular-like upwelling at
330 **$t = t_0$, and permeability function ; b) temporal evolution of the convective pattern showing the detachment of a high temperature « blob » (T > 300°C); c) Plots of vertical temperature profiles taken at the blob vertical axis (red vertical line in the top left pattern) for each time step shown in b). Color-bar (not shown) is the same as in previous figures.**

Starting from the initial stage, deep hot fluid accelerates and finally forms an isolated blob of fast hot fluid, separated from the

335   tail. The black-contoured area in Fig. 7b contains fluid hotter than 300°C. Before the splitting occurs, maximum fluid velocity reaches 3 10^{-7} m.s^{-1} (9 m.yr^{-1}), whereas typical fluid velocity is around 5 10^{-8} m.s^{-1} for a permeability of 5 10^{-15} m² and around 10^{-8} m.s^{-1} for a permeability of 10^{-15} m². Figure 7c illustrates the thermal signature of this ascending blob (or splitting plume). It can be seen that vertical temperature profiles have ~~indeed~~ a negative temperature gradient at t$_0$ + 120 yr and after. The multiple blobs illustrated at t$_0$ + 450–475 yr are also visible on labelled temperature profiles.

5. Results from 3D models

340

In the following, ~~the~~ simplified 3D numerical approach is focused on the case of a finite-size fault zone, embedded in a less permeable host rock. In order to validate our numerical approach and procedure, we first performed benchmark tests on the basis of a recently published study, where different teams worked on the same numerical scenario but with different finite elements numerical codes~~, say OpenGeoSys, Golem and FEFLOW~~ (Magri et al., 2017). As emphasized by the authors, despite

345   similar convective patterns ~~were obtained~~, some quantitative differences in the results were observed, and interpreted as due to « discretization errors (spatial/temporal) » or different « solver settings ». Consequently, our benchmark test is also expected to reproduce qualitatively the same convective patterns ~~as those published by this study~~.

Benchmark tests and results are described in Appendix B. These tests consider a thin (40 m wide) fault zone with simplified

350   fluid properties, identical to those of the Magri et al. (2017) study. In Appendix B, convective patterns, thermal and velocity fields, and temperature anomalies are detailed. The following experiments (below) are focused on the case of thicker permeable fault zones (100–400 m), where the fluid density law is more realistic than in benchmark tests since it is temperature- and pressure-dependent (see Appendix A). The thermal boundary condition at the bottom of the box (depth 5500 m) is not 170 °C as in Magri et al. (2017) and in our benchmark experiment, but corresponds to ~~a~~ more realistic fixed heat flow condition of

355   100 mW.m^{-2}, a typical value in favorable areas for geothermal exploration (e.g. Blackwell et al., 2006; Cloetingh et al., 2010; Erkan, 2015). However, this high basal heat flow will not induce temperature values higher than 210 °C. To involve temperatures around 300-350°C, one would need to impose a basal heat flow condition around 180 mW.m², a value considered as too extreme for the purpose of this study (see however Della-Vedova et al. 2008, where basal heat flow in Tuscany, Italy, would be around 150–200 mW.m²). In the following, the role of ~~a~~ depth-dependent permeability and the effect of the fault dip

360   angle are investigated. To avoid ~~discussing about~~ edge effects, the case of a longer fault is also presented.

5.1 Case of a vertical fault zone with a constant permeability

In the following experiment, which is derived from the benchmark case, the fault zone is 400 m wide, 5 km deep, does not outcrop at the surface and does not reach the bottom of the box (depth 5.5 km). Its dip angle will be varied as well as its

permeability ~~value or variation~~. An averaged heat production of 2 µW.m^{-3} is imposed in the entire model, to account for

365 representative radiogenic heat production in a shallow granitic crust (Jaupart and Mareschal, 2011; Artemieva et al., 2017).

Top left of Fig. 8 shows some of the boundary conditions, the ~~missing~~ others being no flow and no thermal exchanges.
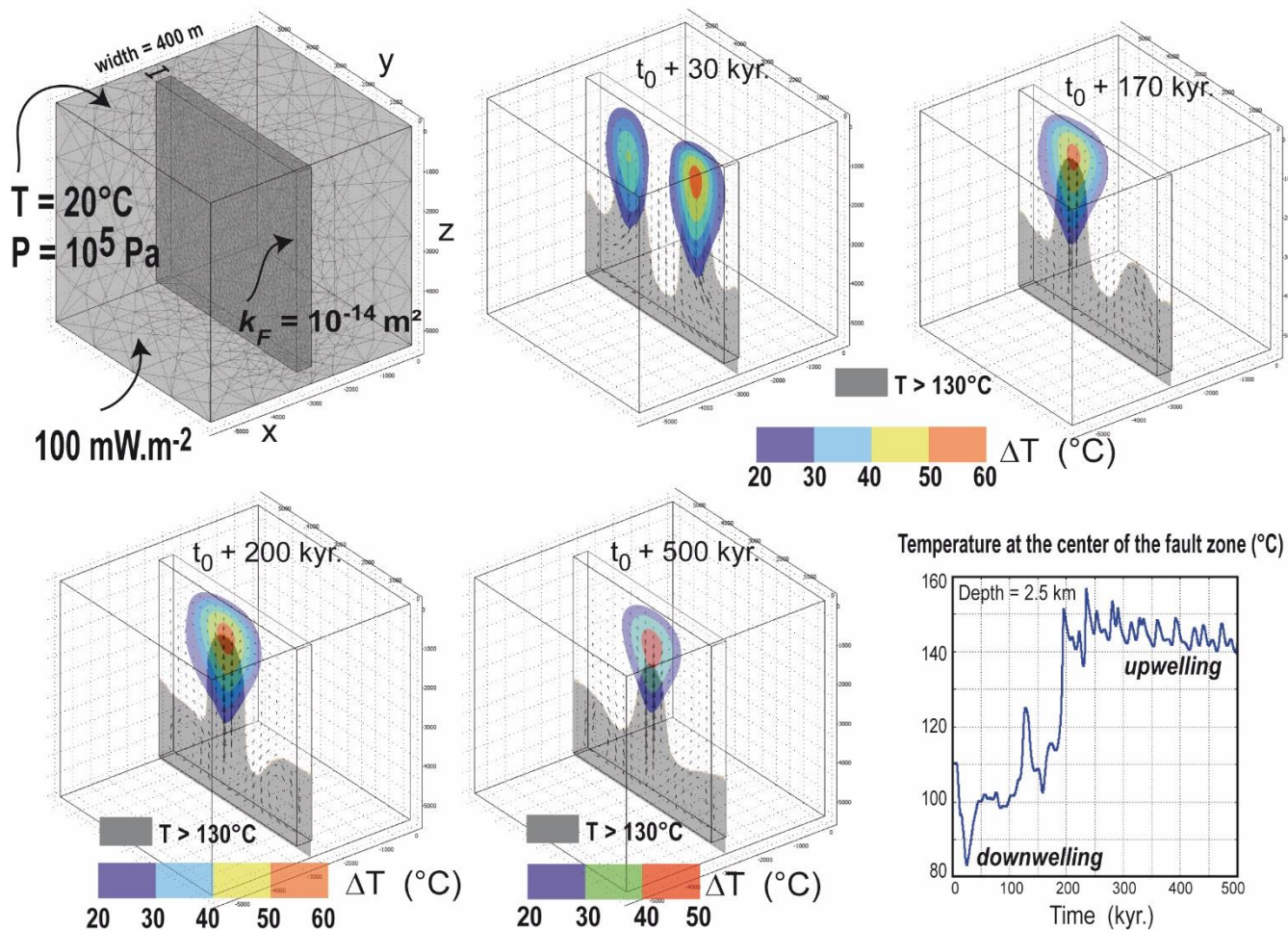
Figure 8. Case of a wide vertical fault zone in a 3D block, with realistic fluid properties and boundary conditions. Fault permeability is fixed at 10^{-14} m². Positive temperature anomalies ~~above~~ 20°C are colored in the middle plane of the fault zone. Zones where
370 **temperature exceeds 130°C are shown in grey. Temperature evolution at the center of the fault zone illustrates the transition from a downwelling to ~~an~~ upwelling, from 150 to 200 kyr.**

In Fig. 8, the fault permeability (k_F) is fixed at 10^{-14} m², while the host rock is supposed impervious (k_H = 10^{-18} m²). Figure 8

illustrates the time evolution of positive temperature anomalies (colored zones, in the middle plane of the fault zone, defined

375 as temperature excess when compared to the conductive case) together with the domain for which temperature is greater than

130°C (grey areas). Time evolution of temperature at a depth of 2.5 km within the fault zone is also shown.

Temperature anomalies in 3D exhibit ~~some kind of~~ « hot air balloon morphology » (see one perpendicular view in ~~the next~~ Fig. 9), where the maximum value exceeds 50°C, for at least 200 kyr. ~~It must be emphasized that~~ this shape was ~~already~~ visible

380 in the benchmark experiment (Appendix B, Fig. B1). This morphology could be ~~assimilated to~~ the "geothermal reservoir", whose size would be described by a given critical value of the temperature anomaly (e.g. $\Delta T > 30$°C). The absolute temperature value at a depth of 2.5 km also exceeds 150°C between 200 and 340 kyr (see temperature evolution in the lower right plot of Fig. 8). During the first 200 kyr., the convective pattern is mainly dominated by a central cold downwelling and two adjacent upwellings. With time, the pattern reverses for ~~promoting a~~ single hot central upwelling.

385 ## 5.2 Similar case for an inclined fault

Figure 9 shows an experiment where all parameters are identical to the previous one, except for the fault dip angle, here chosen at 30° from the vertical. Figure 9b illustrates the temperature field at $t_0 + 200$ kyr, at a depth of 2.1 km (colored plane), where 150 °C is ~~reached at the centre~~; it also shows the distorted 150°C isotherm (in red), ~~emphasiz~~ing the upward fluid circulation, ~~rising~~ at a maximum velocity of $2.4 \ 10^{-8}$ m.s^{-1} (0.75 m.yr^{-1}). Figure 9c illustrates the time evolution of temperature anomalies,

390 from two « balloons » to a single one at times greater than $t_0 + 190$ kyr. During the transition from two to one single upwelling, the temperature anomaly decreases in amplitude, and then recovers values greater than 50°C (see time $t_0 + 215$ kyr). At the bottom left of Fig. 9c, a lateral view of the same temperature anomaly shows that (i) temperature anomaly extends laterally to more than 500 m away from the fault zone boundaries; (ii) the maximum range of [50-60] °C extends in a depth range of ~1.0 to 2.2 km. Figure 9d shows a downward temperature profile along the fault (A-B in Fig. 9a). The upward temperature anomaly

395 is clearly visible and appears to be maximum at time $t_0 + 215$ kyr ~~(at this time, a temperature of 150°C is reached at a depth of 1.5 km, as shown in Fig. 9b)~~.
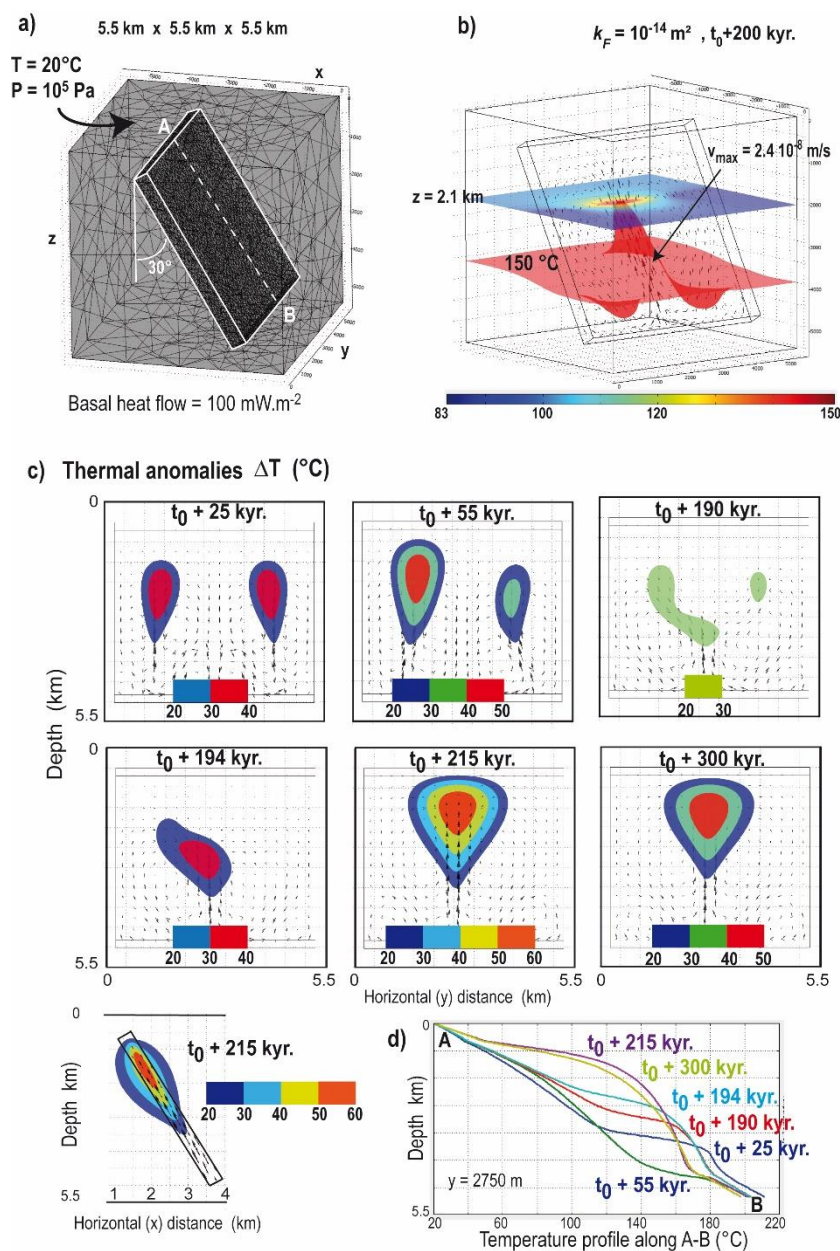
Figure 9. (a) Similar experiment as in Figure 8 but for an inclined (30°) fault zone. (b) a temperature of 150°C is reached at a depth of 2.1 km. Color bar corresponds to temperature values at a depth of 2.1 km; (c) temporal evolution of thermal anomalies (colored zones), viewed in a vertical plane: a similar transition from two upwellings to a single central one is observed. The other perpendicular view in bottom left illustrates lateral diffusion of the anomaly within the host rock; (d) temperature evolution within the fault zone along the A-B profile.

5.3 Cases with a depth-dependent permeability

405   In the four experiments of Fig 10, a depth-dependent permeability (exponential decrease) is imposed within the fault, and the dip angle varies from 0 (vertical) to 45°. The maximum fault permeability is here 20 times higher than in Fig. 8 and 9. For each dip angle, transient evolution of positive thermal anomalies are illustrated with 3 time steps for which particular convective patterns have been selected.
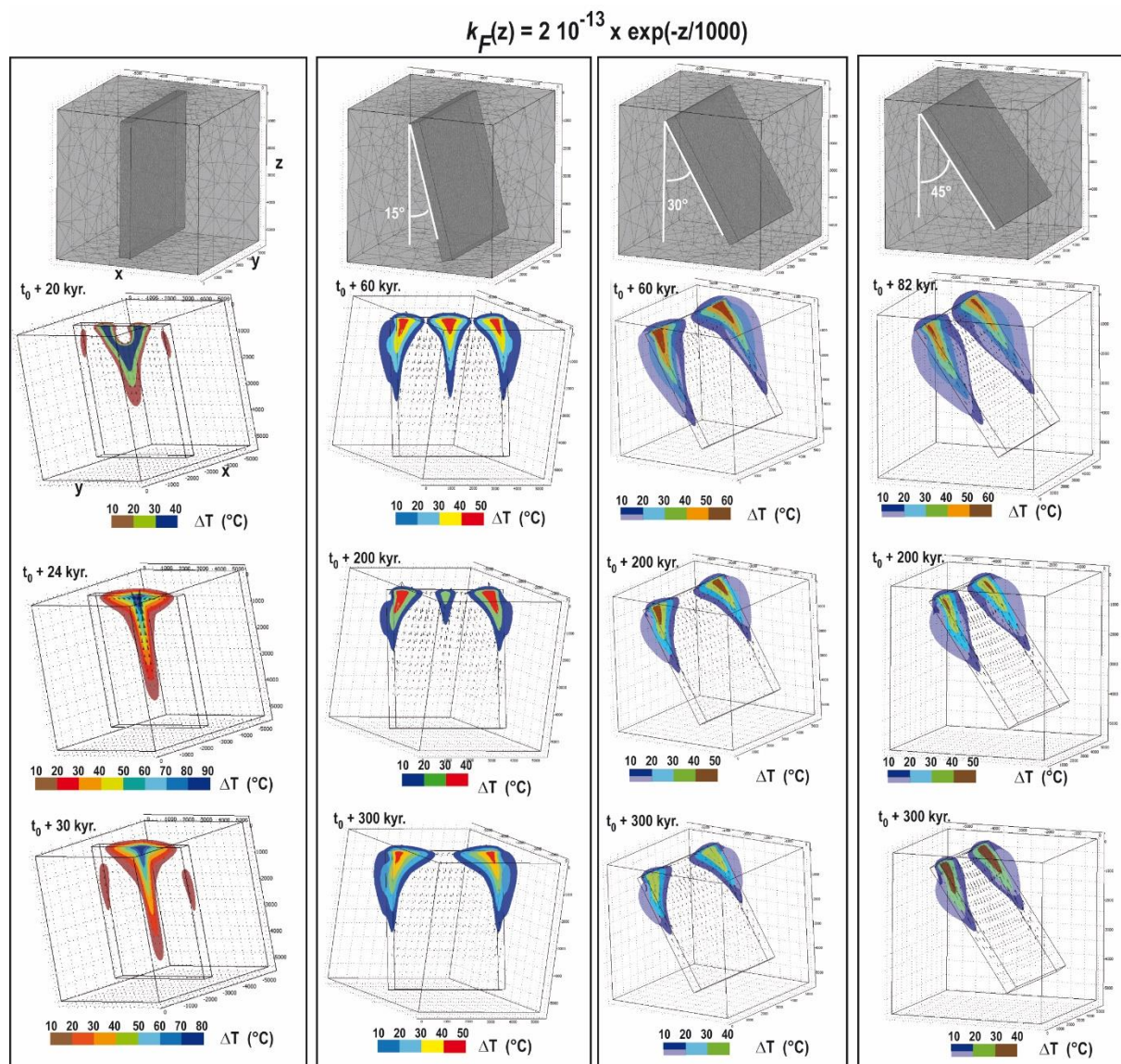
Figure 10. Four experiments with realistic fluid properties and a depth-dependent permeability, with a dip angle of 0, 15, 30 and 45°. Few differences exist between the two last cases. The largest anomaly amplitudes are obtained in the vertical case (left) and during the first tens of kyr. In the second case (15°), a transient anomaly disappears after 200 kyr.

In the case of a vertical fault zone (left column), a quasi steady-state convective pattern is reached at time $t_0 + 24$ kyr. The

415   initial anomaly exhibits a « Y-shape » pattern ($t_0 + 20$ kyr) with a temperature anomaly lower than 40°C. With time, the Y-shape anomaly evolves towards a « funnel-shape » pattern ($t_0 + 30$ kyr) with a much ~~higher value for the~~ temperature anomaly. Because permeability is higher at shallow depths, the anomaly expends laterally near the surface. From the top of the fault zone (at a depth of 500 m) to a depth of ~ 1.0 km, a temperature anomaly greater than 80°C (dark blue zone) and around 500 m wide, establishes. ~~If anomalies greater than 50°C are considered (from light to dark blue), then this distance is more than~~

420   ~~doubled~~.

For the three ~~other~~ cases ~~dealing~~ with inclined fault zones (dip angles of 15, 30 and 45°), time evolution is much longer since steady-state convective patterns ~~establish~~ after 200 kyr. There are two main differences between these 3 experiments and the previous one (i.e. the vertical case). The first is that the number of anomalously warm upwellings ~~has been~~ increased. At time

425    $t_0 + 60$ kyr and for a dip angle of 15°, three anomalies (greater than 40°C) are identified. With time, the central one disappears ~~since~~ a central downwelling establishes, ~~thus~~ leaving two positive anomalies at fault edges. The second major difference ~~deals with~~ the value of temperature anomalies, which do not exceed 50-60°C in the case of an inclined fault zone, ~~whereas it exceeds~~ ~~80°C in the vertical case~~. These results are consistent with the 2D models of Duwiquet et al. (2019), who also found higher thermal anomalies for vertical faut zones.

430   **5.4 Case of a longer fault**

The curved shape of lateral anomalies in Fig. 10 (for inclined fault zones) might be due to side effects since fault length is the same as fault height. The following experiments illustrates the case of a longer (15 km) fault zone, with a maximum permeability of 5 10⁻¹³ m². In Fig. 11, fault width is reduced to 100 m and fault dip angle is varied. In Fig. 12, fault dip angle is fixed at 30° while fault width is varied from 100 to 400 m. Snapshots of experiments correspond to time steps during which

435   thermal anomaly is maximum (see temporal evolution in Fig. 11a, and horizontal temperature profiles in Fig. 11b).

In all experiments, funnel-shaped thermal anomalies develop, ~~as it seems to be~~ controlled by the exponential decrease of fault zone permeability. Except for the vertical case (Fig. 11a), thermal anomalies do not exceed 50°C. The maximum temperature anomaly is reached more rapidly when fault dip angle is small (at $t_0 + 55$ kyr and $t_0 + 56$ kyr for 0 and 15°, respectively) or

440   when fault width is large (at $t_0 + 6.8$ kyr for a 400 m wide fault). The two plots of temporal evolution in Fig. 11a show that the maximum temperature anomaly remains elevated (above 25°C) during ~20 kyr, a duration which could be representative of the lifetime of a geothermal sytem. Obviously, this value ~~must be~~ associated ~~to~~ the ~~chosen~~ permeability distribution.
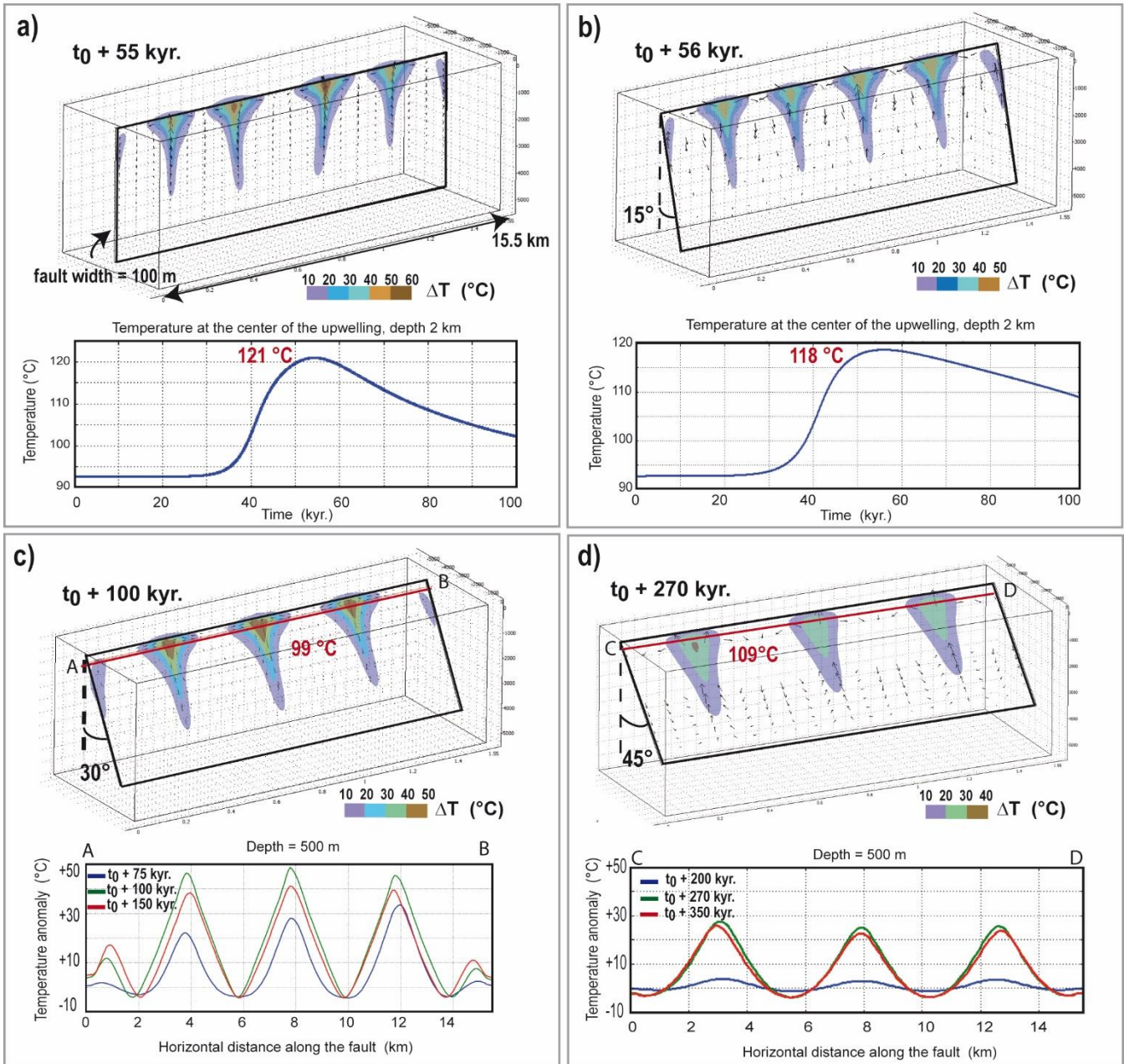
Figure 11. Experiments with a longer (15.5 km long) fault, with different dip angles (0, 15, 30 and 45°). Permeability is depth-dependent with a maximum value of 5 10⁻¹³ m² for each case. The obtained temperature anomalies ~~slightly~~ exceed 50°C in the vertical case only. ~~Each time step~~ illustrates the maximum temperature anomaly obtained during the entire experiment. Time evolution of temperature (top) or temperature anomalies (bottom) are shown beneath temperature anomaly patterns.

Figure 12 shows that the wider the fault, the higher ~~is~~ the number of funnel-shaped anomalies. This results in an almost
450   continuous thermal anomaly at shallow depth (see horizontal profiles at a depth of 350 m, right column of Fig. 12). Figure 13
illustrates thermal diffusion in host rocks: the anomalously high temperatures extend over a distance of 2.4 km (1200 m for
each side). Fig. 13 also illustrates that a vertical fault zone (left case) induces a much higher temperature anomaly (64°C at a
depth of 500 m) than an inclined fault zone (only 38°C on the right case), as already observed in Fig. 10 and 11.
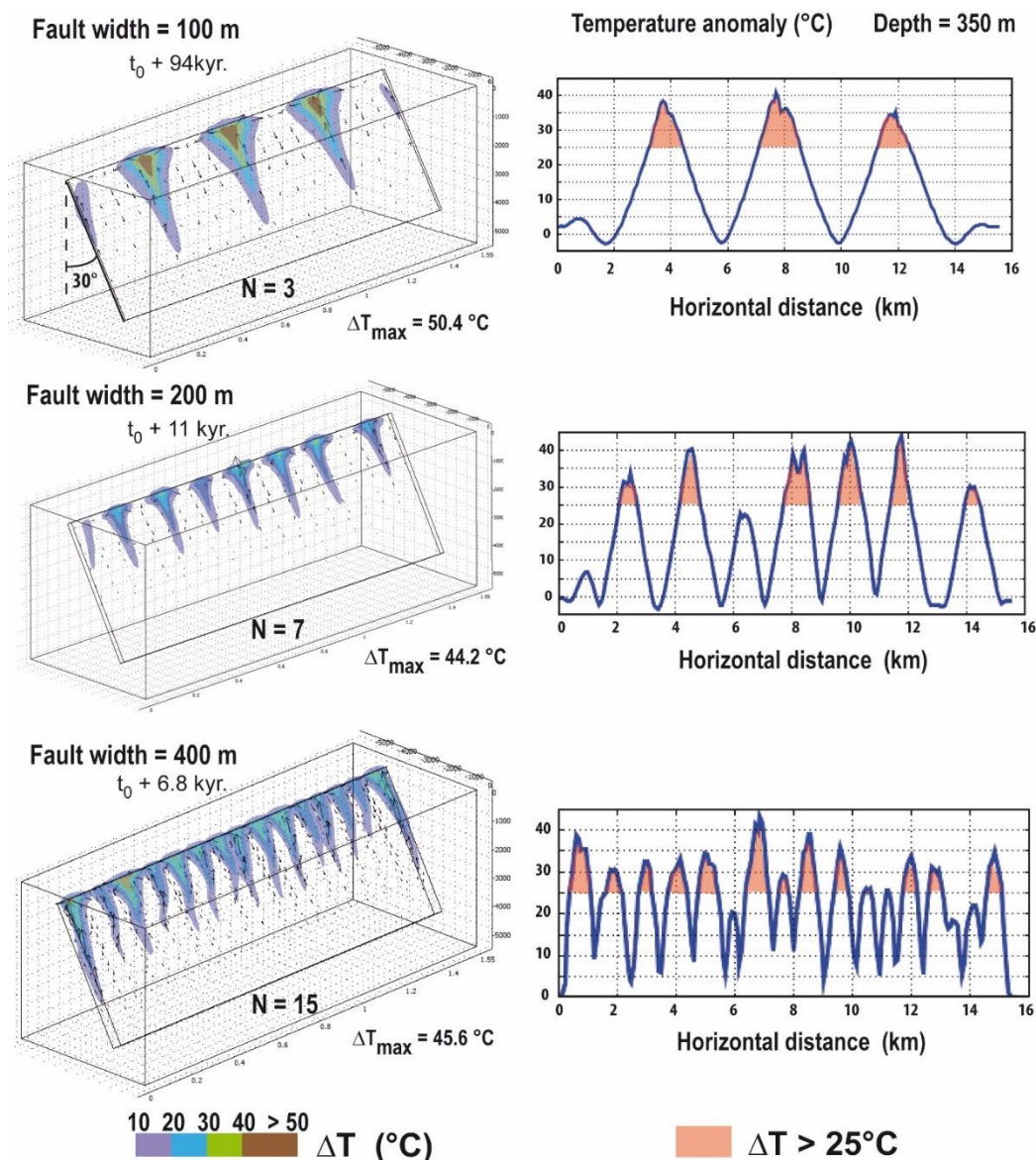
455   **Figure 12. Effect of fault width on temperature anomaly pattern for ~~the same~~ dip angle of 30° and the same permeability law as in
Fig. 11. Values of maximal temperature anomalies are similar, but the wider the fault, the more numerous ~~are~~ the positive thermal
anomalies. Temperature anomalies greater than 25°C at a depth of 350 m are ~~illustrated~~ on the right ~~of each case.~~**
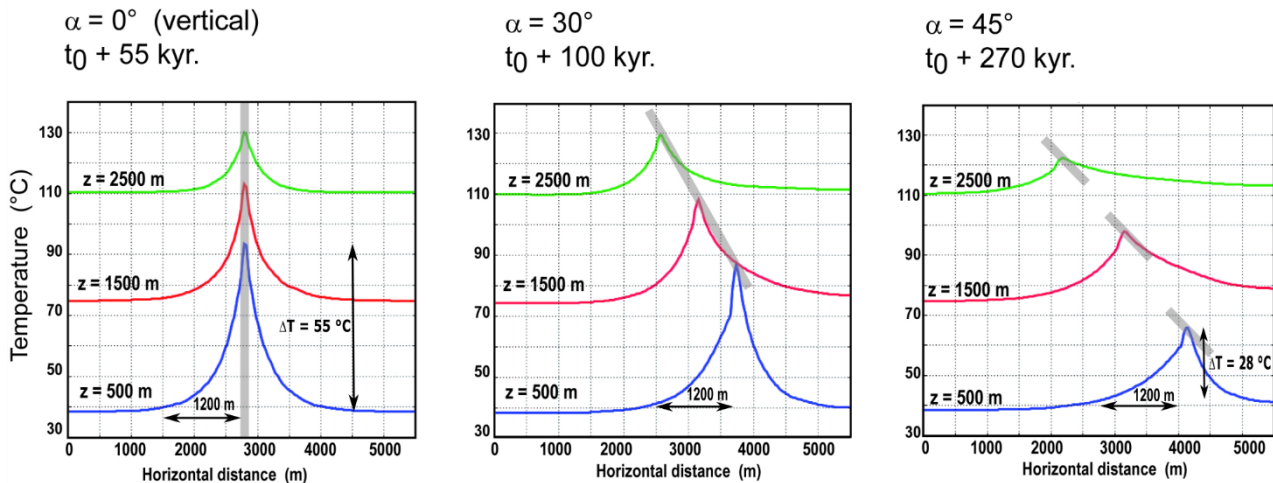
Figure 13. Effect of fault dip angle (the angle is illustrated by grey rectangles) on horizontal profiles of temperature, perpendicular
460 **to the fault zone, at the time when temperature anomaly is maxmum (indicated on top of each case). While the lateral diffusion**
length remains similar (~ 1200 m on each side, at a depth of 500 m, and ~800-900 m at a depth of 2500m), the amplitude is clearly
greater in the vertical case (~55°C at a depth of 500 m in the vertical case, and ~28°C for a dip angle of 45°).

Finally, Fig. 14 shows temporal evolution of thermal anomalies superimposed on the temperature field within a 100 m wide

465 vertical fault zone. Two different permeability fields in the fault zone are illustrated, so that the ratio between fault permeability

and host rocks permeability equals 20 and 50. While only one internal upwelling dominates in the left case, four upwellings

are obtained in the case of the most permeable fault zone. Because fluid velocity is smaller in the first case (the maximum

temperature anomaly is reached at t_0 + 200 kyr, but only at t_0 + 45 kyr in the permeable case), thermal diffusion in the host

rocks occurs into a wider volume (compare the two horizontal map view at the bottom of Fig. 14). Although the along-fault

470 dimension of the two thermal anomalies are similar (2.3 and 2.5 km) their width differ by almost a factor of 2. Another

important difference deal with the amplitude of the maximum temperature anomaly: while it reaches 78°C in the left case, it

only reaches 66°C in the permeable case. Consequently, from these two experiments, one could conclude that the volume and

the potential of the "geothermal reservoir" appears more important for the smaller permeability ratio, which would favor higher

temperatures and wider thermal diffusion, but additional experiments with higher permeability ratios, as in Duwiquet et al.

475 (2019) are required. Actually, one last experiment, not shown here because the imposed basal heat flow was 150 mW.m^{-2}, was

carried out with a permeability ratio of 100. Three funnel-shape anomalies developed with a maximum amplitude of 120°C

centered at 500 m depth. For this particular experiment, temperatures of 150°C were reached at a depth of 750 m. Temperature

anomalies exceed 70°C over a depth range of 3 km and a lateral dimension of 700 m.
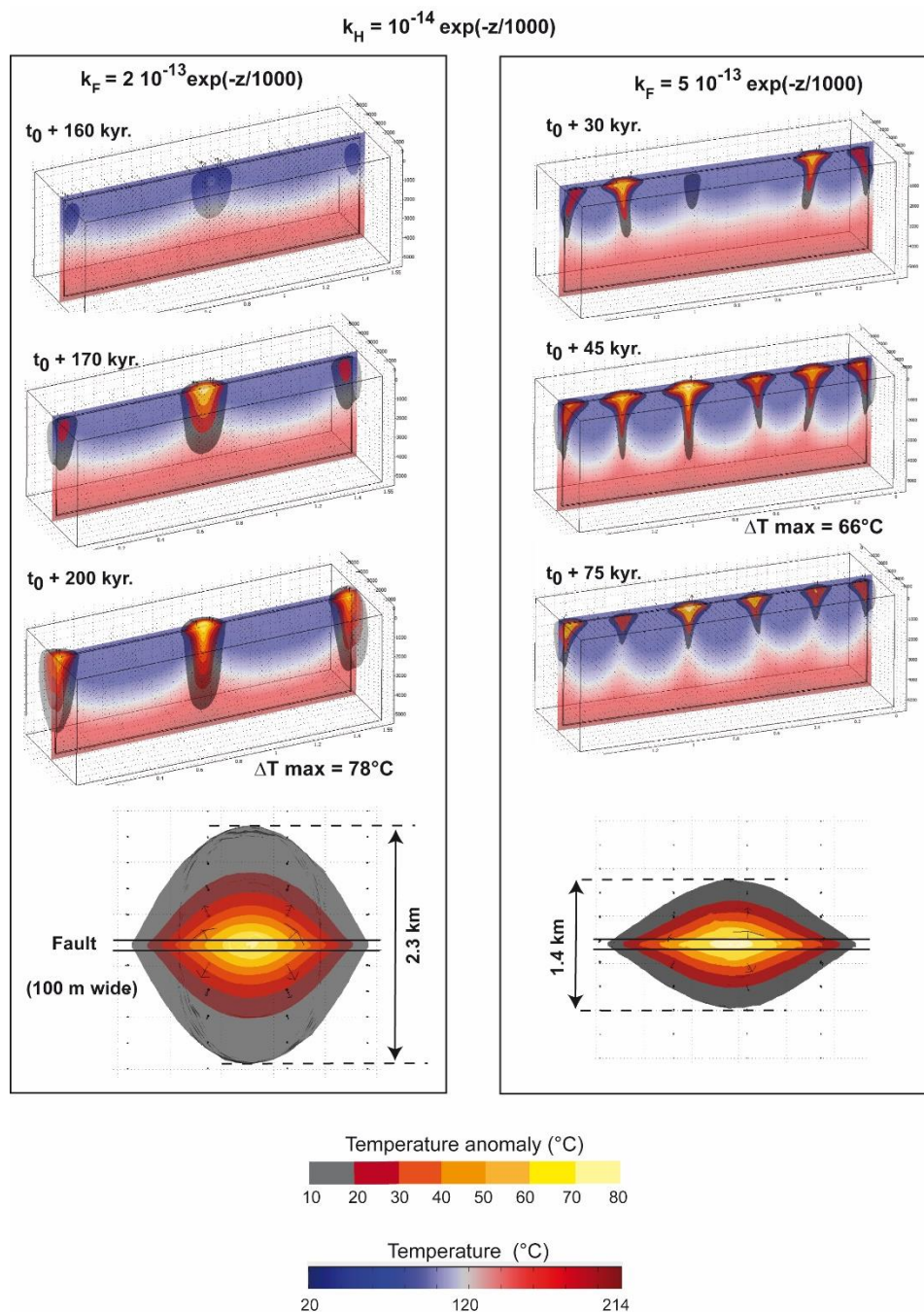
Figure 14. Effect of permeability ratio between the vertical fault zone and the host rocks: $k_F/k_H = 20$ (left) and 50 (right). Maximum temperature anomaly is reached at time t_0+ 200 kyr (left) and t_0 + 45 kyr (right). Bottom figures show temperature anomalies from above at a depth of 500 m. While the maximum amplitudes of the anomalies do not differ much (66 and 78°C), the lateral diffusion lengths strongly differ (2.3 and 1.4 km wide).

6 Discussion

The main objective of this study ~~consisted in~~ investigating the various possible convective patterns and the associated thermal anomalies in a permeable fault zone. ~~The~~ 2D experiments were first performed to validate our numerical approach by reproducing the published results ~~by~~ Rabinowicz et al. (1998), and can be viewed as fluid circulation models along a fault plane, without accounting for ~~the embeddings~~. Some particular processes ~~have been underlined~~ (such as the thermal inheritance mechanism) and are discussed below. When more realistic fault zones are considered, i.e. when damage zones of several tens to hundreds of meters are taken into account, 3D experiments are required since convective patterns are expected to also depend on host rock properties. In 2D experiments, boundary conditions and fluid properties were chosen to reproduce the results by Rabinowicz et al. (1998) and fluid density law ~~was~~ in particular simplified (Appendix A). In 3D experiments, more realistic physical conditions are applied: fluid density is temperature- and pressure-dependent, and the bottom thermal boundary condition corresponds to a fixed heat flow of 100 mW.m^{-2}.

6.1 2D convective patterns

In the first series of 2D models, the well-known finger-like convective pattern was reproduced for a constant permeability (Fig. 1). Because of lithostatic pressure, permeability decreases with depth and the use of a more realistic permeability distribution appears to change the finger-like pattern towards a triangular-like pattern (Fig. 2) with a dominant cooling effect. Indeed, the most permeable levels being at shallow depths, cold downwellings are favored. This may explain why, along permeable fault zones, hot upwellings (evidenced by emergence of thermal springs) are not numerous and irregularly spaced.

Actually, ~~e~~quivalent effects ~~are obtained in~~ presence of ~~an important~~ topography (> 1500 m) ~~since~~ infiltrating cold fluids ~~at high altitude~~ dominate and prevent hot fluids ~~to~~ rise ~~at~~ the surface, except in a few locations (see the clusters of thermal springs in the Pyrenees, in Taillefer et al., 2017). The role of topography on the location of ~~clusters of~~ thermal springs in the Jordan rift valley has also been investigated by Magri et al. (2015), who illustrated the ~~possible~~ coexistence of topography-driven ~~flow~~ and buoyancy-driven flow. ~~Consequently, our results should not be considered as soon as topography is important since~~ topography-driven flow ~~may~~ predominate and modify the convective patterns. Nevertheless, the results shown in Fig. 2 indicate that when topography is not important, ~~the~~ depth-dependent permeability may have similar consequences ~~as a significant topography~~.

In Fig. 3 and 4, ~~the~~ instantaneous and continuous increases of permeability modify the initial convective pattern (triangular-like or finger-like) to form bulb-like convective patterns, with a significant temperature increase at shallow depth. Conversely, ~~the~~ decrease in permeability ~~allows~~ recovering the finger-like pattern, accompanied by ~~a~~ short-duration cooling ~~event~~ (Fig. 4). This process might be of major importance for geothermal exploration around active fault zones, where permeability is

probably at its maximum. In other words, active fault zones could host geothermal reservoirs with a kilometer-scale bulb-like geometry (see also Patterson et al., 2018a; Wanner et al., 2019).

The thermal inheritance concept illustrated in Fig. 5 and 6 may be relevant for a number of geological processes involving
520 circulation of deep hot fluids. Studies on gold metallogeny (orogenic gold deposits, BIF-hosted gold deposits) have often suggested polyphased mineralizing events (e.g. Bonnemaison and Marcoux, 1990; Lawley et al., 2015; Gourcerol et al., 2020). This mechanism could indeed be at the origin of polyphased hydrothermal ore deposits in the sense that a structure already mineralized could be more favourable for focussing the latter hydrothermal stages. It must be noted that while "structural inheritance" was invoked many times to explain strain localization or tectonic history of mountain belts (e.g. Jammes et al.,
525 2013), thermal inheritance appears as another physical mechanism that may play an important role in the wide range of thermo-mechanical processes.

Finally, the splitting behavior observed in Fig. 7 has been used by Deveaud et al. (2015) to suggest one possible dynamical mechanism at the origin of rare-elements pegmatite emplacement. Indeed, these fluent-rich magmatic liquids have an
530 extremely low viscosity (e.g. Bartels et al., 2013). Consequently, the associated dynamic permeability (the ratio between static permeability and fluid viscosity) is anomalously high, and their escape and detachment from a deep crustal magma source through permeable shear zones is facilitated. Successive separations from a magma source could represent an alternative process to explain the differences in chemical enrichment within a single pegmatite field (Melleton et al., 2015). In addition, the splitting behaviour may represent one way to expulse hot blobs of magma that would crystallize away from their source, a
535 mechanism which could help resolving the "pegmatite paradox" (Butler and Torvela, 2018). In addition to thermal inheritance, this pulsating behaviour observed in Fig. 7 was also suggested by Link et al. (2019) to explain the multiphase gold mineralizing events in fault zones of the Pyrenees, south of France.

6.2 3D hydrothermal convection and temperature anomalies

540 The understanding of 3D hydrothermal convection in fault zones made some important progress in the last decades. Recently, a new Rayleigh number expression based on fault geometry and on physical fluid and rock properties has been proved to be more adapted than the Rayleigh theory to define the onset of thermal convection (Malkovski and Magri, 2016). As far as numerical modeling of 3D hydrothermal convection is concerned, numerous geological examples have been studied, from the fractured oceanic lithosphere to fault zones (e.g. Rabinowicz et al., 1998; Fontaine et al., 2001; Zhao et al., 2003; Bächler et
545 al., 2003; Kuhn et al., 2006; Baietto et al., 2008; Harcouët-Menou et al., 2009; Coumou et al., 2009; McLellan et al., 2010; Person et al., 2012; Magri et al., 2016; Malkovski and Magri, 2016; Magri et al., 2017; Taillefer et al., 2018; Patterson et al., 2018a; Patterson et al., 2018b; Bauer et al., 2019). For each case, some surprising dynamical features were discovered, like

the thermal interference between separated fractures (Patterson et al., 2018b), or the helicoidal fluid flow pathways (Magri et al., 2016). However, the anomalously high temperatures at shallow depths were not necessarily studied in detail.

550

Patterson et al. (2018a) have reproduced typical convective patterns such as those described in our 3D benchmark tests (Fig. B1), but for thinner fractures (up to 10 m wide) of elliptical geometry. The values of their obtained temperature anomalies (see their Fig. 3) are at least twice lower (not greater than ± 15°C) than those obtained in our benchmark tests, where fault width equals 40 m. However, geometry of their thermal anomalies remains similar and shows a "hot air balloon" morphology. Person et al. (2012) illustrated the role of fault intersections on temperature anomalies at the surface, for fault permeability values ranging from 2 to 7 10^{-13} m². Transient evolution shows that temperature anomalies up to 92°C can be achieved. Yet, in their experiments, fault widths are small (10 and 20 m), but a « spring » thermal boundary condition (no vertical temperature gradient) was imposed at the surface, in the lowlands of their model, including the vertical fault zones. This boundary condition should probably favor upflow of deep hot fluids within these highly permeable structures and their temperatures anomalies might be overestimated. Our 3D models show that without imposing a spring condition at the surface, temperature anomaly up to 90°C may indeed settle at the top of a non-outcropping vertical fault zone (Figure 10, vertical case).

According to previous studies where width of the fault zone is smaller than 100 m, and with our results where widths exceed 100 m, it seems that the wider the fault, the higher is the temperature anomaly: around 30°C for a 40 m wide fault zone (Appendix B); around 50–60°C when fault width equals or exceeds 100 m, (e.g. Fig. 11) and up to 80-90 °C when the fault zone is wide and vertical (Fig. 10, left and Fig. 14). Nevertheless, this is not the case in Fig. 12, where only fault zone width varies, from 100 to 400 m, and where temperature anomaly.remains around 50 ± 10 °C. Actually, the most important parameter could be the fault dip angle, as illustrated in Fig. 10, and as already suggested by Achtziger-Zupančič et al. (2016). However, permeability distribution plays clearly a role, and it is probably the combination between fault width, fault permeability distribution and dip angle which controls the amount of energy towards the surface (e.g. Roche et al., 2019). A more systematic study on all these parameters should allow to build a regime diagram for 3D convective patterns.

6.3 Morphology of thermal anomalies

The amount of energy has been recently illustrated by Wanner et al. (2019) who modelled the effect of a vertical upflow in a permeable (10^{-13} m²) zone (area of 150 m ×100 m). They obtained an ellipsoidal vertical thermal plume providing 120°C at a depth of 2 km. Morphology of their thermal anomaly is close to our "hot air balloon" morphologies (Fig. 8 an 9), although boundary conditions differ: in their model, an overpressure is imposed at the base of the upflow zone, and a fixed temperature of 4°C is imposed on the top surface, preventing any lateral expansion of the anomaly (our funnel-shaped anomalies). The fact that we obtained a temperature of 150°C at a depth of 2.1 km w (Fig. 9b., where fault zone permeability is 10^{-14} m²) may be due to buoyancy-driven flow, which does not appear to play a role in the Wanner et al. (2019) study. This difference may also

be due to the different boundary conditions and initial thermal regimes. Nonetheless, ~~the~~ lateral thermal diffusion of the anomaly is obtained in both cases, thus defining the lateral dimension (2-4 km) of a geothermal reservoir.

The "hot air balloon" morphology can also be seen in the Patterson et al. (2018a) study where temperature perturbations vary
585 according to the imposed fault permeability. It can be seen in their Fig.3 that thermal diffusion in the host rocks results in anomalies of quasi-circular shape, similar to what is shown in Appendix B (Fig. B2b). In our experiments, the "hot air balloon" morphology was not the unique shape. Indeed, the "funnel-shape" anomalies illustrated for instance in Fig. 10, 11, 12 and 14, seem to dominate as soon as fault permeability is depth-dependent and convection sufficiently vigorous. As already mentioned, it is difficult to use the Rayleigh number theory to define the "vigor" of the convection, but clearly, one can see that convective
590 patterns are more and more disturbed when fault permeability increases, when fault width increases and when fault dip angle is close to zero. As an example, the quasi-circular shape obtained in map view (e.g. Fig. B2b, but also in Fig. 14, bottom left), becomes more ovoid when permeability ratio between the fault zone and the host rocks is increased. Indeed, in that case, fluid velocity being higher, the host rocks are less imprinted by the hot rising fluid, and diffusion of the thermal anomaly extends over a smaller distance (bottom right of Fig. 14). This process may have important consequences on geothermal exploration
595 since the interesting volume where thermal anomalies could be exploited (the geothermal reservoir) may strongly depend on permeability ratio.

6.4 Permeability ratio

As ~~already~~ mentioned by several studies, and observed here again, temperature is not necessarily ~~the~~ adequate parameter to
600 describe hydrothermal convection (Fig. 1) and to define which convective regime will dominate. ~~According to Börsing et al. (2017) and Niederau et al. (2019), enthalpy or entropy production could be more appropriate.~~ Indeed, Fig. 1 (2D models) as well as Fig. 14 (3D models) illustrate that temperature values do not necessarily increase regularly when permeability increases. As pointed out by several authors (e.g. Lopez and Smith, 1995 ; Baietto et al., 2008), permeability ~~of the embeddings~~ is also important. In a recent compilation of measured or inferred permeability values in fault zones, Scibek (2020) indicates, when
605 available, the permeability ratio between the fault zone and ~~the embeddings.~~ Duwiquet et al. (2019) suggested a regime diagram for different 2D convective patterns as a function of permeability ratios. However, permeability ratio is probably also depth-dependent. In Fig. 14, the same depth-decrease of permeability has been chosen so that a permeability ratio of 20 and 50 can be defined, but it may not be representative of real fault zones, where the depth-decrease is probably more important in the surrounding rocks. The question whether fault zone permeability remains elevated at depth is crucial, since it may ~~involve~~
610 upwellings of deep hot fluids at shallow depths. According to Achtziger-Putančič et al. (2017), that might be the case for dense networks of overlapping fault damage zones.

6.5 Amplitude and diffusion of thermal anomalies

As shown in Fig. 14, the horizontal cross sections of the anomaly may differ ~~for two~~ different permeability ratio. Indeed, the fastest the fluid can rise, the shorter is the time ~~period during which~~ thermal diffusion ~~occurs within~~ the host rock. ~~It is~~

615 ~~important, h~~owever, ~~to note that~~ the maximum amplitude of the anomaly is similar in both cases of Fig. 14 (78 and 66°C). Hence, for these ~~2~~ experiments, permeability ratio does not seem to play a significant role on the amplitude of the anomaly. ~~On the opposite,~~ Fig. 13 shows that fault dip angle seems to control the amplitude of the anomaly: at the depth of 500m (blue curves), the amplitude reaches 55°C for the vertical case (left) and then decreases down to 28°C for a dip angle of 45°C. ~~On the other hand, t~~he thermal diffusion length remains the same for the three cases (~ 1200 m at a depth of 500 m). This length

620 scale is in line with the results of lateral heating deduced by Wustefeld et al. (2017), and with spatial distribution of paleotemperature estimates measured on carboneous material by Link et al. (2019) across an auriferous shear zone.

6.6 Limits and perspectives

These preliminary 3D experiments of hydrothermal convection in fault zones, based on a successful benchmark test, have been simplified (no topography, geometry ~~of the fault zone~~, homogeneous host rocks, no time-dependence of permeability, fluid

625 properties of pure water) in order to investigate the role of a few parameters on convective processes. As emphasized by many authors (e.g. Ingebritsen and Appold, 2012; Ague, 2014), hydrothermal convection is complex, and the fact that we account for the fault dip angle in addition to the 3D geometry and the depth-dependent permeability was considered as a sufficiently elaborate~~d~~ model. Clearly, it would be worth to perform 3D experiments related to real-case studies including surface topography, fault intersections and other key geological features ~~being prone to disturb the convective patterns identified in~~

630 ~~this study~~. When ~~such kind of~~ approaches ~~were performed~~, one objective was to reproduce – for instance – the location and temperature of thermal springs, or temperature and heat flow data (e.g. Magri et al., 2015; Magri et al., 2016; Taillefer et al., 2019; Roche et al., 2018; Duwiquet et al., 2019). This is not the case ~~of~~ our study which is focused on the physical processes leading to the establishment of thermal anomalies at shallow depths.

635 The first 2D models reproduced ~~mechanisms involving~~ high temperatures (> 300 °C) since they were based on benchmark tests resulting from models of hydrothermal convection in oceanic ridges (Rabinowicz et al., 1998). For 3D models of fault zones, a more realistic basal heat flow of 100 mW.m^{-2} was assumed, but temperatures did not exceed 214°C. Further modelling may have to consider deeper systems (e.g. crustal fault zones reaching at least a depth of 10 km) involving temperatures that would be present around the brittle-ductile transition.

640

Another ~~next~~ step for further 3D models should account for dynamic (time-dependent) permeability, since transient unexpected changes in the convective patterns were obtained in the 2D models (e.g. Fig. 3 and 4). For example, one may observe transitions from "hot air balloon" morphology in the case of a low permeability, to funnel-shape patterns after a sudden permeability

increase. In addition, only 2 permeability ratios were investigated (Fig. 14), whereas many authors demonstrated that it
645   represents a major parameter being able to modify discharge temperatures and local heat flux (e.g. Lopez and Smith, 1995;
Baietto et al. 2008; Duwiquet et al., 2019). It is thus probable that different morphologies (not only funnel-shaped) could
appear when permeability ratio is varied over a wider range.

Finally, it is well known that fluid composition (especially its salinity) strongly affects the density variation with temperature
650   and pressure (Weis et al., 2014). Our simplified choice of using pure water density law consists in giving a starting frame for
investigating possible morphologies of thermal anomalies, but more realistic density law should be incorporated in future
studies. Consequently, our results can probably be applied to crustal fault zones away from strong topography and which are
not related to an underlying magmatic system (non-magmatic geothermal systems, Moeck, 2014).

7 Conclusion

655   The aim of this work was to investigate the respective role of different parameters on the shape and locations of thermal
anomalies induced by hydrothermal convection in permeable fault zones. Through idealized and simplified 2D and 3D
numerical models, a series of different convective patterns were obtained, depending mainly on (i) spatial and temporal
variations of permeability and (ii) fault zone thickness and dip angle. Some new thermal processes identified in 2D (thermal
inheritance, splitting plumes with a pulsating behaviour) were not tested in 3D but should clearly represent the research
660   objectives of further 3D modelling studies. Nevertheless, our preliminary 3D results have shown that thermal anomalies, either
of "funnel" shape or of "hot air ballon" morphology, can easily exceed 50°C over a depth range of one kilometer. In the case
of vertical fault zones, temperature anomalies mais reach 80-90°C and those greater than 30°C can extend laterally over more
than 1 km from the fault boundary.

665   Although it was not possible to isolate a single controlling parameter, it appears that the amplitude of positive thermal
anomalies is more important when the fault zone is vertical. If one exploration guide would have to be defined from these
preliminary results, one would clearly opt for the vertical fault zones. However, fluid velocity in vertical fault zone may be so
high that thermal diffusion would have no time to heat significantly the surrounding rocks. A subtle balance between
permeability of the fault zone and that of the embeddings, may result in a large volume of anomalously hot rocks, thus creating
670   interesting targets for geothermal exploration.

Appendices

Appendix A: Governing equations, fluid and rock properties and numerical procedure

675   In this study, numerical simulations of hydrothermal convection have been performed with the Comsol Multiphysics™ software (finite element method), by coupling Darcy law, heat equation and mass conservation. Details on these equations can be found in Guillou-Frottier et al. (2013). Three different fluid and rock properties have been used in the simulations. First, for 2D experiments, same fluid and rock properties as in Rabinowicz et al. (1998) have been chosen in order to reproduce some of their results (Figure 1d and 1f). For example, the fluid density law for these 2D experiments is:

680

$$\rho_L(T) = 1036.5 - 1416.7\ 10^{-4} \times T - 2238.1\ 10^{-6} \times T^2 \tag{A1}$$

where subscript L means liquid, where density ρ_L is in kg.m^{-3}, and temperature T is in °C.

Second, for 3D benchmark experiments (see Appendix B), which refer to published results by Magri et al. (2017), same
685   physical properties have been chosen. In particular, the density law varies linearly with temperature and is written, in the 0-150 °C domain:

$$\rho_L(T) = 1022.38 \times (1 - 0.00059 \times (T - 20)) \tag{A2}$$

where T is in °C.

690

Third, for the other 3D experiments (Fig. 8 to 14), more realistic fluid and rock properties have been used. Indeed, fluid density law is not only temperature-dependent but also pressure-dependent. The chosen fluid density law corresponds to a polynomial function, fitting experimental data for pure water and for temperature and pressure ranges of 0–1000 °C and 0–500 MPa (NIST Chemistry Webbook, Linstrom and Mallard, 2001; Launay, 2018) :

695

$$\rho_L(T,P) = 1006 + (7.424 \times T) + (-0.3922 \times P) + (-4.441\ 10^{-15} \times T^2)) + (4.547\ 10^{-9} \times T \times P) + (-0.003774 \times P^2) + (-1.451\ 10^{-23} \times T^3) + (-1.793\ 10^{-17} \times T^2 \times P) + (2.955\ 10^{-6} \times P^3) + (-1.463\ 10^{-32} \times T^4) +$$
$$(-1.361\ 10^{-26} \times T^3 \times P) + (4.018\ 10^{-21} \times T^2 \times P^2) + (-7.372\ 10^{-15} \times T \times P^3) + (5.698\ 10^{-11} \times P^4) \tag{A3}$$

700   where temperature T is in °C and pressure P in Pa. The fluid viscosity is only temperature-dependent and follows the exponentional decrease as given in Rabinowicz et al. (1998):

$$\mu\ (T) = 2.414\ 10^{-5}\ \times 10^{\frac{247.8}{(T+133)}} \tag{A4}$$

705 where viscosity μ is in Pa.s and T in °C. All other properties of the fluid are identical as those used in many studies: heat capacity $Cp_L = 4180$ J.kg^{-1}.K^{-1}, thermal conductivity of the liquid $k_L = 0.6$ W.m^{-1}.K^{-1}. Host rock properties are also typical for granitic rocks: density of the solid (S) $\rho_S = 2700$ kg.m^{-3}, heat capacity $Cp_S = 800$ J.kg^{-1}.K^{-1}, thermal conductivity $k_S = 3.0$ W.m^{-1}.K^{-1}, heat production rate $A = 2$ µW.m^{-3}. It must be pointed out that absolute values of these physical properties are not critical since permeability values can vary by several orders of magnitude and thus largely control the regime of hydrothermal

710 convection.

Porosity in the host rock is taken at 1% while it amounts to 20% in the fault zone. Classic mixing rules are used for defining equivalent heat capacity and thermal conductivity of the saturated medium (see equations 5 and 6 in Guillou-Frottier et al., 2013). Here again, the absolute values of porosity do not greatly influence the hydrothermal regime when compared to the

715 chosen permeability values.

In most models, transient evolution is computed until a steady-state is reached. While initial pressure field always corresponds to a hydrostatic gradient, the initial thermal regime varies from one case to the other, in particular when thermal inheritance is studied (Fig. 5 and 6). When a pure conductive regime is taken as the initial condition, the analytical expression accounting

720 for heat production is applied to the entire model and inserted in the numerical code:

$$T_0(z) = T_0 + \left(\frac{Q_b + A \times H}{k}\right) \times z - \left(\frac{A}{2k}\right) \times z^2 \qquad (A5)$$

where T_0 is the imposed surface temperature, Q_b the imposed basal heat flow, A the heat production rate, H the height of the

725 model, k the equivalent thermal conductivity and z is depth from the top surface. By definition, the "temperature anomaly" is defined by the computed temperature minus the equilibrium conductive temperature given in (A5). When a non-conductive state is chosen as an initial condition (e.g. Fig. 7), the obtained solution from a previous run is implemented as the new initial condition.

730 For the first 2D models (Fig. 1), numerical mesh consists in 6726 triangles, with a maximum size of 20 m. Same mesh parameters have been used for longer models (Fig. 6). For the 3D models, size of tetrahedrals is refined within the fault zone, down to a maximum size of 100 m for cases with high permeability or with a large fault zone: in the case of Fig. 11 and 14b, the total number of tetrahedras equals 31819, with a maximum size of 100 m within the fault zone.

735 Within the Comsol Multiphysics™ software, hydrothermal convection equations are solved with an automatically chosen direct linear solver (e.g. UMFPACK in version 3.5, PARDISO in version 5.4), and time discretization is also automatically

chosen so that absolute and relative tolerance are satisfied. However, in the case of too low tolerance values, several distinct solutions can be obtained when mesh size or the imposed time stepping is modified. To avoid the possibility of getting different solutions when time stepping or mesh size are modified, relative and absolute tolerances have been set to 10^{-5} and 10^{-6},

740 respectively. This strong constraint allowed getting stable and robust solutions, as confirmed by the 3D benchmark experiments (Appendix B).

Appendix B: 3D Benchmark tests

For the 3D benchmark experiments, the same fluid properties as those used in Magri et al. (2017) have been imposed (linear

745 temperature-dependence for density law, and exponential decrease of viscosity with temperature, see their Fig. 1b and Appendix A). Rock (fault and host rock) properties are also the same. Transient evolution is computed up to $t_0 + 10^{13}$ s, as in their Fig. 5. It must be specified that an error appeared in the published results of 2D experiments in Magri et al. (2017): medium permeability was not "1.019 10^{-13} m²" but around 1-5 10^{-15} m² (Magri, pers. comm., 2019). This value allowed us to reproduce the 2D results (not shown here) including their fluid velocity pattern (their Fig. 3), but with a maximum velocity

750 value of 1.4 10^{-9} m.s^{-1} and not 2.8 10^{-6} m.s^{-1}. Similarly, the published 3D result in their Fig. 5 indicates minimum and maximum temperature perturbations of "± 32°C" instead of -20.62 °C and 28.94 °C (Magri, pers. comm., 2019). The correct temperature range is given in Fig. B1.

Figure B1 shows the 3D benchmark experiment performed with OpenGeoSys (left figure, Magri, pers. comm., 2019) and with

755 Comsol Multiphysics™ (our study, right figure). All boundary conditions are the same, and geometries are identical (fault width is 40 m). The results shown in Fig. B1 correspond to time $t_0 + 10^{13}$ s. Convective patterns are identical but temperature anomalies differ by 1 and 3 °C for minimum and maximum values, respectively. As explained by Magri et al. (2017), numerical instabilities may easily develop in density-driven flow problems. In addition, time discretization adpoted by Comsol Multiphysics™ may also differ from that imposed in the other numerical codes.

760

Figure B2 illustrates some additional details of the convective regime within the fault. Fluid velocity pattern is shown in Fig. B2a, temperature anomalies viewed from above at different depths are shown in Fig. B2b, and temperature anomalies from sections perpendicular to the fault are shown in Fig. B2c. Interestingly, despite fault width is small (40 m), thermal anomalies diffuse over hundreds of meters (and even thousands of meters if values different from the conductive regime are accounted

765 for).
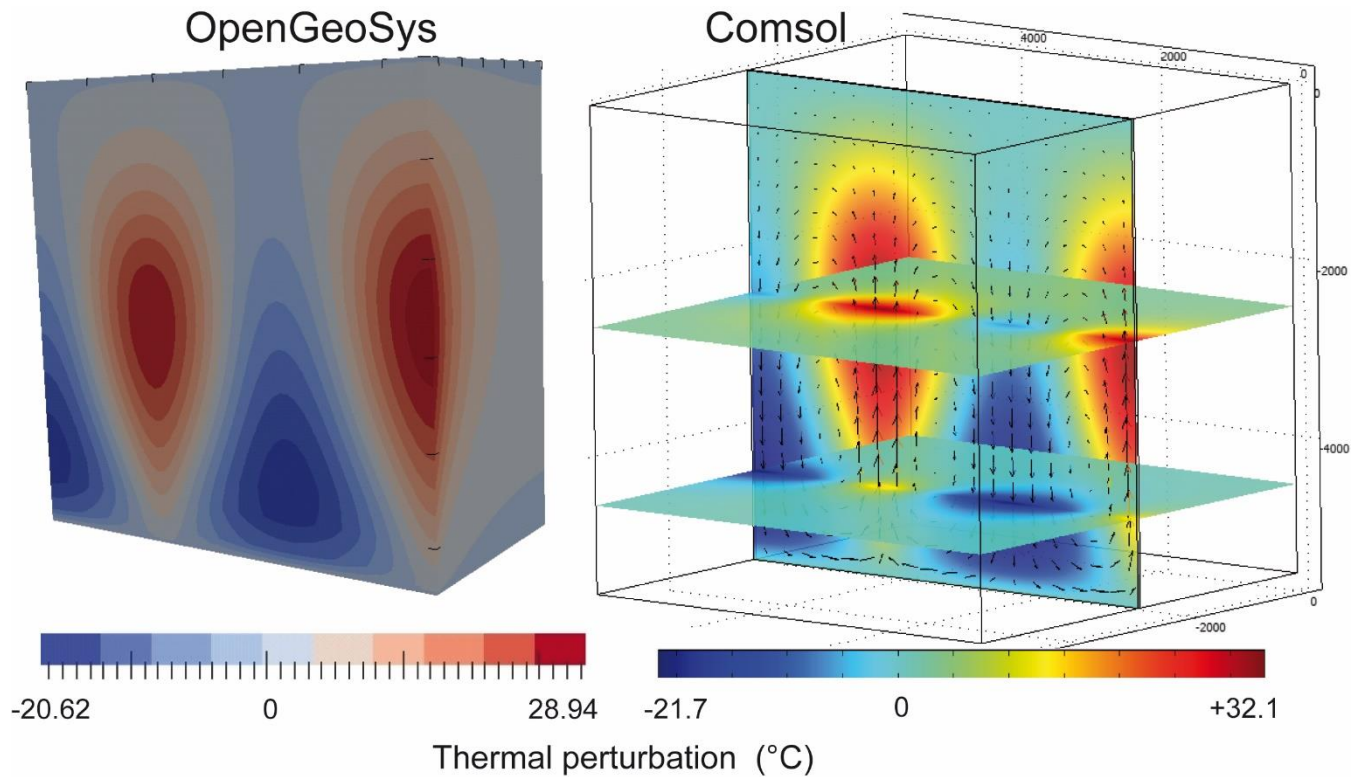
Figure B1. Benchmark experiment for a 40 m wide fault zone embedded in impervious host rock (cube of 5.5 km), as in the Magri et al. (2017) study (left). Our result (right) indicates slight differences in temperature perturbation (see text) but convective pattern is identical.
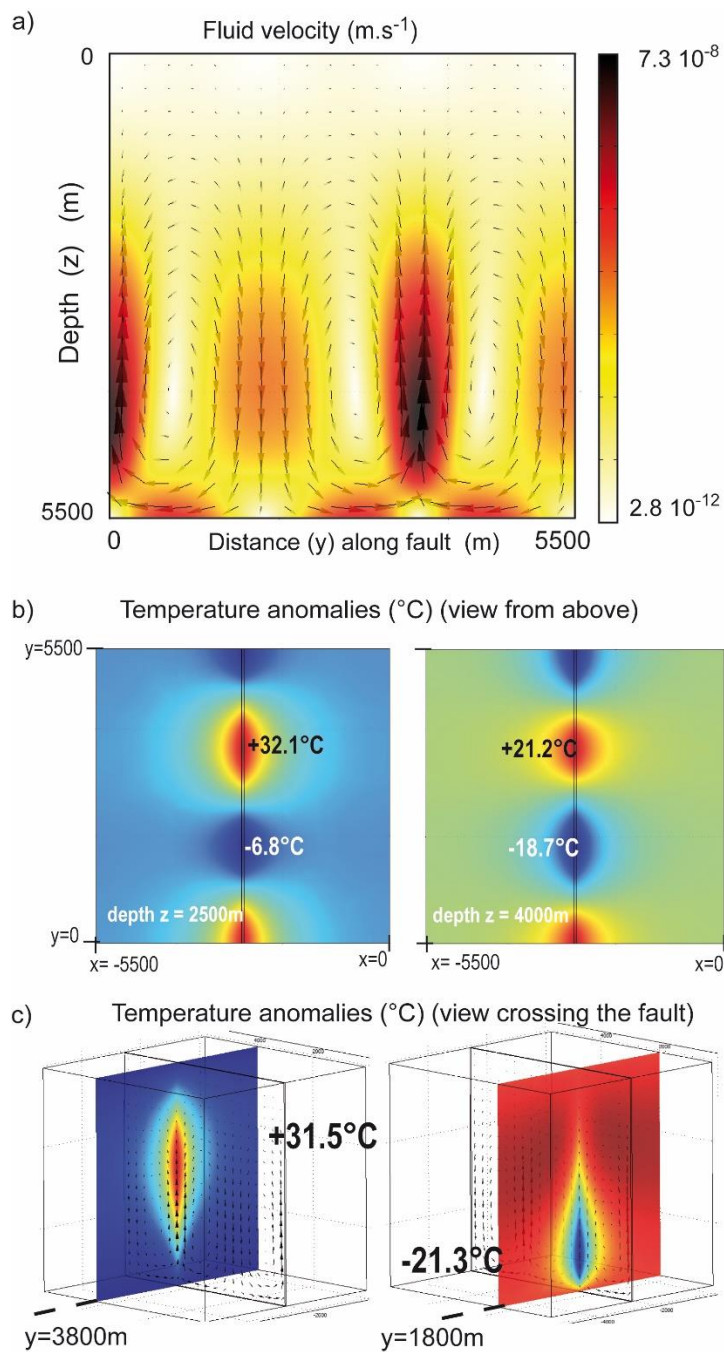
Figure B2. Details on the 3D benchmark experiment of Figure B1. a) Field velocity and values within the fault ; b) lateral diffusion of temperature anomalies at depths 2500 and 4000 m ; c) lateral diffusion of hot and cold anomalies, perpendicularly to the fault.

775

Code availability

The numerical codes are available upon request to the first author.

Author contribution

HD, GL, AT, VR and GL contribute to this work through their PhD theses on fluid circulation in permeable fault zones. HD
780 and LGF developed the 3D model, GL implemented the density law. LGF wrote the initial draft and all co-authors contribute
to the writing of the final manuscript.

Competing interest

The authors declare that they have no conflict of interest.

Special Issue statement

785 **Acknowledgements**

We would like to thank Pr. Fabien Magri for fruitful discussions and for running again his 3D benchmark experiment to answer
our questions. This study was partly funded by the Labex Voltaire (ANR-10-LABX-100-01) homed at Orléans University and
BRGM, the French Geological Survey.

790

References

Achtziger-Putančič, P., Loew, S., Hiller, A., and Mariethoz, G.: 3D fluid flow in fault zones of crystalline basement rocks (Poehla-Tellerhaeuser Ore Field, Ore Mountains, Germany), Geofluids, 16, 688-710, https://doi.org/10.1111/gfl.12192 2016.

795 Achtziger-Putančič, P., Loew, S., and Hiller, A.: Factors controlling the permeability distribution in fault vein zones surrounding granitic intrusions (Ore Mountains/Germany), J. Geophys. Res., 122, 1876-1899, https://doi.org/10.1002/2016JB013619 2017.

Ague, J.J.: Fluid flow in the deep crust, Treatise on geochemistry, 2nd edition, 203-247, https://doi.org/10.1016/B0-08-043751-6/03023-1 2014.

800 Artemieva, I.M., Thybo, H., Jakobsen, K., Sorensen, N. K., Nielsen, L.S.K.: Heat production in granitic rocks: Global analysis based on a new data compilation GRANITE2017, Earth Sci. Rev., 172, 1-26, https://doi.org/10.1016/j.earscirev.2017.07.003 2017.

Bächler, D., Kohl, T., and Rybach, L.: Impact of graben-parallel faults on hydrothermal convection – RhineGraben case study, Phys. Chem. Earth, 28, 431-441, https://doi.org/10.1016/S1474-7065(03)00063-9 2003.

805 Baietto, A., Cadoppi, P., Martinotti, G., Perello, P., Perrochet, P., and Vuataz, F.-D.: Assessment of thermal circulations in strike–slip fault systems : the Terme di Valdieri case (Italian western Alps), Geol. Soc. Spec. Pub., 299, 317-339, https://doi.org/10.1144/SP299.19 2008.

Bartels, A., Behrens, H., Holtz, F., Schmidt, B.C., Fechtelkord, M., Knipping, J., Crede, L., Baasner, A., and Pukallus, N.: The effect of fluorine, boron and phosphorus on the viscosity of pegmatite forming melts, Chem. Geol., 346, 184-198,
810 https://doi.org/10.1016/j.chemgeo.2012.09.024 2013

Bauer, J.F., Krumbholz, M., Luijendijk, E., and Tanner, D. C.: A numerical sensitivity study of how permeability, porosity, geological structure, and hydraulic gradient control the lifetime of a geothermal reservoir, Solid Earth, 10, 2115-2135, https://doi.org/10.5194/se-10-2115-2019 2019.

Bense, V. F., Gleeson, T., Loveless, S. E., Bour, O., and Scibek, J.: Fault zone hydrogeology, Earth Sci. Rev., 127, 171-192,
815 https://doi.org/10.1016/j.earscirev.2013.09.008 2013.

Blackwell, D.D., Netragu, P.T., and Richards, M.: Assessment of the Enhanced Geothermal System resource base of the United States, Natur.Resources Res., 15, 283-308, https://doi.org/10.1007/s11053-007-9028-7 2006

Boiron M.-C., Cathelineau, M., Banks, D. A., Fourcade, S., and Vallance, J. : Mixing of metamorphic and surficial fluids during the uplift of the Hercynian upper crust: consequences for gold deposition, Chem. Geol., 194, 119-141,
820 https://doi.org/10.1016/S0009-2541(02)00274-7 2003.

Bonnemaison, M., and Marcoux, E.: Auriferous mineralization in some shear-zones: A three-stage model of metallogenesis, Mineral. Deposita, 25, 96–104, https://doi.org/10.1007/BF00208851 1990.

Bonté, D., Guillou-Frottier, L., Garibaldi, C., Bourgine, B., Lopez, S., Bouchot, V., and Lucazeau, F.: Subsurface temperature maps in French sedimentary basins: new data compilation and interpolation, Bull. Soc. Geol. Fr., 181, 377-390,
825   https://doi.org/10.2113/gssgfbull.181.4.377 2010.

Börsing, N., Wellmann, J. F., Niederau, J., and Regenauer-Lieb, K. : Entropy production in a box: analysis of instabilities in confined hydrothermal systems, Water Resour. Res., 53,7716-7739, https://doi.org/10.1002/2017WR020427 2017.

Butler, R.W.H, and Torvela, T.: The competition between rates of deformation and solidification in syn-kinematic granitic intrusions: resolving the pegmatite paradox, J. Struct. Geol., 117, 1-13, https://doi.org/10.1016/j.jsg.2018.08.013 2018.

830   Clauser, C., and Villinger, H.: Analysis of conductive and convective heat transfer in a sedimentary basin, demonstrated for the Rheingraben, Geophys. J. Int., 100, 393-414, https://doi.org/10.1111/j.1365-246X.1990.tb00693.x 1990.

Cloetingh, S., van Wees, J.D., Ziegler, P.A., Lenkey, L., Beekman, F., Tesauro, M., Förster, A., Norden, B., Kaban, M., Hardebol, N., Bonté, D., Genter, A., Guillou-Frottier, L., TerVoorde, M., Sokoutis, D., Willingshofer, E., Cornu, T., and Worum, G.: Lithosphere tectonics and thermo-mechanical properties: An integrated modelling approach for Enhanced
835   Geothermal Systems exploration in Europe, Earth Sci. Rev., 102, 159-206, https://doi.org/10.1016/j.earscirev.2010.05.003 2010.

Coumou, D., Driesner, T., Geiger, S., Heinrich, C. A., and Matthäi, S.: The dynamics of mid-ocean ridge hydrothermal systems: splitting plumes and fluctuating vent temperatures, Earth Planet. Sci. Lett., 245, 218-231, https://doi.org/10.1016/j.epsl.2006.02.044 2006.

840   Coumou, D., Driesner, T., Geiger, S., Paluszny, A., and Heinrich, C.A.: High-resolution three-dimensional simulations of mid-ocean ridge hydrothermal systems, J. Geophys. Res., 114, B07104, https://doi.org/10.1029/2008JB006121 , 2009.

Coelho, G., Branquet, Y., Sizaret, S., Arbaret, L., Champallier, R., and Rozenbaum, O.:..Permeability of sheeted dykes beneath oceanic ridges: Strain experiments coupled with 3D numericalmodeling of the Troodos Ophiolite, Cyprus. Tectonophysics, 644-645, 138-150, https://doi.org/10.1016/j.tecto.2015.01.004 2015.

845   Cox, S.F.: The application of failure mode diagrams for exploring the roles of fluid pressure and stress states in controlling styles of fracture-controlled permeability enhancement in faults and shear zones, Geofluids, 10, 217-233, https://doi.org/10.1111/j.1468-8123.2010.00281.x 2010.

Curewitz, D. and Karson, J.A.: Structural settings of hydrothermal outflow: Fracture permeability maintained by fault propagation and interaction, J. Volcanol. Geotherm. Res.,79, 149-168 https://doi.org/10.1016/S0377-0273(97)00027-9
850   1997.

Della Vedova, B., Vecellio, C., Bellani, S., and Tinivella, U.: Thermal modelling of the Larderello geothermal field (Tuscany, Italy), Int. J. Earth Sci., 97, 317–332, https://doi.org/0.1007/s00531-007-0249-0 2008.

Deveaud, S., Guillou-Frottier, L., Millot, R., Gloaguen, E., Branquet, Y., Villaros, A., Pichavant, M., and Barbosa da Silva, D.: Innovative and multi-disciplinary approach for discussing the emplacement of Variscan LCT-pegmatite fields, Proceedings of the 13th SGA Biennal Meeting, Nancy, France, 24-27 August 2015, Vol. 2, 717-720, 2015

Duwiquet, H., Arbaret, L., Guillou-Frottier, L., Heap, M. J., and Bellanger, M.: On the geothermal potential of crustal fault zones: a case study from the Pontgibaud area (French Massif Central, France), Geotherm. Energy, 2019, 7-33, https://doi.org/10.1186/s40517-019-0150-7 2019.

Erkan, K.: Geothermal investigations in western Anatolia using equilibrium temperatures from shallow boreholes, Solid Earth, 6, 103-113, https://doi.org/10.5194/se-6-103-2015 2015.

Fairley, J. P., and Hinds, J. J., Rapid transport pathways for geothermal fluids in an active Great Basin fault zone, Geology, 32, 825-828, https://doi.org/10.1130/G20617.1 2004.

Faulds, J., Coolbaugh, M., Bouchot, V., Moeck, I., and Oğuz, K.: Characterizing structural controls of geothermal reservoirs in the Great Basin, USA, and western Turkey: developing successful exploration strategies in extended terranes, Proceedings World Geothermal Congress, Bali, Indonesia, 25-29 April 2010, 11 p., 2010.

Faulkner, D.R., Jackson, C.A.L., Lunn, R.J., Schlische, R.W., Shipton, Z.K., Wibberley, C.A.J., and Withjack, M.O.: A review of recent developments concerning the structure, mechanics and fluid flow properties of fault zones, J. Struct. Geol, 32, 1557-1575, https://doi.org/10.1016/j.jsg.2010.06.009 2010.

Fehn, U., Cathles, L., and Holland, H.D.: Hydrothermal convection and uranium deposits in abnormally radioactive plutons, Econ. Geol., 73, 1556-1566, https://doi.org/10.2113/gsecongeo.73.8.1556 1978.

Fontaine, F. J., Rabinowicz, M., and Boulègue, J.: Permeability changes due to mineral diagenesis in fractured crust: implications for hydrothermal circulation at mid-ocean ridges, Earth Planet. Sci. Lett., 184, 407-425, https://doi.org/10.1016/S0012-821X(00)00332-0 2001.

Forster, C., and Smith, L.: The influence of groundwater flow on thermal regimes in mountainous terrain: a model study, J. Geophys. Res., 94, 9439-9451, https://doi.org/10.1029/JB094iB07p09439 1989.

Garibaldi, C., Guillou-Frottier, L., Lardeaux, J.-M., Bonté, D., Lopez, S., Bouchot, V., and Ledru, P.: Thermal anomalies and geological structures in the Provence basin: implications for hydrothermal circulations at depth, Bull. Soc. Geol. Fr., 181, 363-376, https://doi.org/10.2113/gssgfbull.181.4.363 2010.

Gerdes, M., Baumgartner, L. P., and Person, M.: Convective fluid flow through heterogeneous country rocks during contact metamorphism, J. Geophys. Res., 103, 23983-24003, https://doi.org/10.1029/98JB02049 1998.

Gourcerol, B., Kontak, D.J., Petrus, J.A. and Thurston, P.C.: Application of LA ICP-MS analysis of arsenopyrite to gold metallogeny of the Meguma Terrane, Nova Scotia, Canada, Gondwana Res., 81, 265-290, https://doi.org/10.1016/j.gr.2019.11.011 2020.

Guillou-Frottier, L., Carré, C., Bourgine, B., Bouchot, V., and Genter, A.: Structure of hydrothermal convection in the Upper Rhine Graben as inferred from corrected temperature data and basin-scale numerical models, J. Volcanol. Geotherm. Res., 256, 29-49, https://doi.org/10.1016/j.jvolgeores.2013.02.008 2013.

Harcouët-Menou, V., Guillou-Frottier, L., Bonneville, A., Adler, P. M., and Mourzenko, V.: Hydrothermal convection in and around mineralized fault zones: insights from two- and three-dimensional numerical modeling applied to the Ashanti belt, Ghana, Geofluids, 9, 116-137, https://doi.org/10.1111/j.1468-8123.2009.00247.x 2009.

890 Horne, R. N., Three-dimensional natural convection in a confined porous medium heated from below, J. Fluid Mech., 92, 751-766, https://doi.org/10.1017/S0022112079000860 1979.

Howald, T., Person, M., Campbell, A., Lueth, V., Hofstra, A., Sweetkind, D., Gable, C.W., Banerjee, A., Luijendijk, E., Crossey, L., Karlstrom, K., Kelley, S., and Philipps, F.M.: Evidence for long timescale (>103 years) changes in hydrothermal activity induced by seismic events, Geofluids, 15, 252-268, https://doi.org/10.1111/gfl.12113 2015.

895 Hutnak, M., Hurwitz, S., Ingebritsen, S. E., and Hsieh, P. A.: Numerical models of caldera deformation: Effects of multiphase and multicomponent hydrothermal fluid flow, J. Geophys. res., 114, B04411, https://doi.org/10.1029/2008JB006151 2009.

Ingebritsen, S.E., and Appold, M.S.: The physical hydrogeology of ore deposits, Econ. Geol., 107, 559-584, https://doi.org/10.2113/econgeo.107.4.559 2012.

Ingebritsen, S. E., and Gleeson, T.: Crustal permeability : introduction to the special issue, Geofluids, 15, 1-10,
900 https://doi.org/10.1111/gfl.12118 2015.

Jammes, S., Huismans, R.S., and Muñoz, J.A.: Lateral variation in structural style of mountain building:controls of rheological and rift inheritance, Terra Nova, 26, 201-207, https://doi.org/10.1111/ter.12087 2013.

Jamtveit, B., Putnis, C.V., and Malthe-Sorenssen, A.: Reaction induced fracturing during replacement processes, Contrib. Mineral. Petrol., 157, 127-133, https://doi.org/10.1007/s00410-008-0324-y 2009.

905 Jaupart, C., and Mareschal, J.-C.: Heat generation and transport in the Earth, Cambridge University Press, 464 p., 2011.

Jupp, T., and Schultz, A., A thermodynamic explanation for black smoker temperatures, Nature, 403, 880-883, https://doi.org/10.1038/35002552 2000.

Kuhn, M., Dobert, F., and Gessner, K.: Numerical investigation of the effect of heterogeneous permeability distributions on free convection in the hydrothermal system at Mount Isa, Australia, Earth Planet. Sci. Lett., 244, 655-671,
910 https://doi.org/0.1016/j.epsl.2006.02.041 2006.

Lapwood, E.R.: Convection of a fluid in a porous medium, Math. Proc. Cambridge Philos. Soc., 44, 508–521, https://doi.org/10.1017/S030500410002452X 1948.

Launay, G. Hydrodynamique des systèmes minéralisés péri-granitiques : étude du gisement à W-Sn-(Cu) de Panasqueira (Portugal). PhD thesis, University of Orléans, France, 514 p., https://tel.archives-ouvertes.fr/tel-02101051 2018.

915 Launay, G., Sizaret, S., Guillou-Frottier, L., Fauguerolles, C., Champallier, R., and Gloaguen, E.: Dynamic permeability related to greisenization reactions in Sn-W ore deposits: quantitative petrophysical and experimental evidence., Geofluids, 2019, Article ID 5976545, 23 pages, https://doi.org/10.1155/2019/5976545 2019.

Lawley, C.J.M., Creaser, R.A., Jackson, S.E., Yang, Z., Davis B.J., Pehrsson, S.J., Dubé, B., Mercier-Langevin, P., and Vaillancourt, D.: Unraveling the western Churchill Province Paleoproterozoic gold metallotect: constraints from Re-Os
920 arsenopyrite and U-Pb xenotime geochronology and LA-ICP-MS arsenopyrite trace element chemistry at the BIF-hosted

Meliadine gold district, Nunavut, Canada, Econ. Geol., 110, 1425-1454, https://doi-org.insu.bib.cnrs.fr/10.2113/econgeo.110.6.1425 2015.

Lin, G., Zhao, C., Hobbs, B.E., Ord, A., and Mühlhaus, H. B.: Theoretical and numerical analyses of convective instability in porous media with temperature-dependent viscosity, Commun. Numer. Meth. Eng., 19, 787–799, https://doi.org/10.1002/cnm.620 2003.

Link, G., Vanderhaeghe, O., Béziat, D., de Saint Blanquat, M., Munoz, M., Estrade, G., Guillou-Frottier, L., Gloaguen, E., Lahfid, A., Melleton, J.: Thermal peak detected in gold-bearing shear zones by a thermo-structural study: a new tool to retrieve fluid flow ?, Proceedings of the 15th SGA Biennal Meeting, Glasgow, Scotland, 27–30 August 2019, Vol. 1, 260–263, 2019.

Linstrom, P.J., and Mallard, W.G.: The NIST Chemistry WebBook : a chemical data resource on the internet, J. Chem. Eng. Data, 46, 1059-1063, https://doi.org/10.1021/je000236i 2001.

Lopez, D. L., and Smith, L., Fluid flow in fault zones: Analysis of the interplay of convective circulation and topographically driven groundwater flow, Water Resour. Res., 31, 1489-1503, https://doi.org/10.1029/95WR00422 1995.

Lopez, T., Antoine, R., Kerr, Y., Darrozes, J., Rabinowicz, M., Ramillien, G., Cazenave, A., and Genthon, P.: Subsurface Hydrology of the Lake Chad Basin from Convection Modelling and Observations, Surv. Geophys., 37, 471-502, https://doi.org/10.1007/s10712-016-9363-5 2016.

Louis, S., Luijendijk, E., Dunkl, I., Person, M.: Episodic fluid flow in an active fault, Geology, 47, 938-942, https://doi.org/10.1130/G46254.1 2019.

Lowell, R.P., Van Cappellen, P., and Germanovich L.N.: Silica Precipitation in Fractures and the Evolution of Permeability in Hydrothermal Upflow Zone, Science, 260, 5105, 192-194, https://doi.org/10.1126/science.260.5105.192 1993.

Magri, F., Inbar, N., Siebert, C., Rosenthal, E., Guttman, J., and Möller, P.: Transient simulations of large-scale hydrogeological processes causing temperature and salinity anomalies in the Tiberias Basin, J. Hydrol., 520, 342-355, http://dx.doi.org/10.1016/j.jhydrol.2014.11.055 2015.

Magri, F., Möller, S., Inbar, N., Möller, P., Raggad, M., Rödiger, T., Rosenthal, E., and Siebert, C.: 2D and 3D coexisting modes of thermal convection in fractured hydrothermal systems - Implications for transboundary flow in the Lower Yarmouk Gorge, Mar. Petroleum Geol., 78, 750-758, https://doi.org/10.1016/j.marpetgeo.2016.10.002 2016.

Magri, F., Cacace, M., Fischer, T., Kolditz, O., Wanf, W., and Watanabe, N.: Thermal convection of viscous fluids in a faulted system : 3D benchmark for numerical codes, Energy Proc., 125, 310-317, https://doi.org/10.1016/j.egypro.2017.08.204 2017.

Malkovski, V. I., and Magri, F.: Thermal convection of temperature-dependent viscous fluids within three-dimensional faulted geothermal systems: estimation from linear and numerical analyses, Water Resour. Res., 52, 1-13, https://doi.org/10.1002/2015WR018001 2016.

Manning C.E., and Ingebristen, S.E.: Permeability of the continental crust: implications of geothermal data and metamorphic systems, Rev. Geophys., 37, 127-150, https://doi.org/10.1029/1998RG900002 1999.

955   McKenna J. R., and Blackwell, D. D., Numerical modeling of transient Basin and Range extensional geothermal systems, Geothermics, 33, 457-476, https://doi.org/10.1016/j.geothermics.2003.10.001 2000.

McLellan, J. G., Oliver, N. H. S., Hobbs, B. E., and Rowland J. V.: Modelling fluid convection stability in continental faulted rifts with applications to the Taupo Volcanic Zone, New Zealand, J. Volcanol. Geotherm. Res., 190, 109-122, https://doi.org/10.1016/j.jvolgeores.2009.11.015 2010.

960   Melleton, J., Gloaguen, E., Frei, D.: Rare-elements (Li-Be-Ta-Sn-Nb) magmatism in the European Variscan belt, a review, Proceedings of the 13th SGA Biennal Meeting, Nancy, France, 24-27 August 2015, Vol. 2, 807-810, 2015.

Mezri, L., Le Pourhiet, L., and Burov, E.: New parametric implementation of metamorphic reactions limited by water content, impact on exhumation along detachment faults, Lithos, 236-237, 287-298, https://doi.org/10.1016/j.lithos.2015.08.021 , 2015.

965   Micklethwaite, S., Ford, A., Witt, W., and Sheldon, H. A.: The where and how of faults, fluids and permeability – insights from fault stepovers, scaling properties and gold mineralisation, Geofluids, 15, 240-251, https://doi.org/10.1111/gfl.12102 2015.

Moeck, I.S.: Catalog of geothermal play types based on geologic controls, Renew. Sustain. Ener. Rev., 37, 867-882, http://dx.doi.org/10.1016/j.rser.2014.05.032 2014.

970   Niederau, J., Wellmann, J. F., and Börsing, N.: Analyzing the influence of correlation length in permeability on convective systems in heterogeneous aquifers using entropy production, Geotherm. Energy, 2019, 7-35, https://doi.org/10.1186/s40517-019-0151-6 2019.

Patterson, J. W., Driesner, T., Matthai, S., and Tomlinson, R.: Heat and fluid transport induced by convective fluid circulation within a fracture or fault, J. Geophys. Res., 123, https://doi.org/10.1002/2017JB015363 2018a.

975   Patterson, J. W., Driesner, T., and Matthai, S. K.: Self-organizing fluid convection patterns in an en echelon fault array, Geophys. Res. Lett., 45, 4799-4808, https://doi.org/10.1029/2018GL078271 2018b.

Pepin, J., Person, M., Phillips, F., Kelley, S., Timmons, S., Owens, L., Witcher, J., and Gable, C.: Deep fluid circulation within crystalline basement rocks and the role of hydrologic windows in the formation of the Truth or Consequences, New Mexico low-temperature geothermal system, Geofluids, 15, 139-160, https://doi.org/10.1111/gfl.12111 2015

980   Person, M., Hofstra, A., Sweetkind, D., Stone, W., Cohen, D., Gable, C. W., and Banerjee, A.: Analytical and numerical models of hydrothermal fluid flow at fault intersections, Geofluids, 12, 312-326, https://doi.org/10.1111/gfl.12002 2012.

Rabinowicz, M., Boulègue, J., and Genthon, P.: Two- and three-dimentional modeling of hydrothermal convection in the sedimented Middle Valley segment, Juan de Fuca Ridge, J. Geophys. Res., 103, 24045-24065, https://doi.org/10.1029/98JB01484 1998.

985   Roche, V., Sternai, P., Guillou-Frottier, L., Menant, A., Jolivet, L., Bouchot, V., and Gerya, T.: Emplacement of metamorphic core complexes and associated geothermal systems controlled by slab dynamics, Earth Planet. Sci. Lett., 498, 322-333, https://doi.org/10.1016/j.epsl.2018.06.043 2018.

Roche, V., Bouchot, V., Beccaletto, L., Jolivet, L., Guillou-Frottier, L., Tuduri, J., Bozkurt, E., Oguz, K., and Tokay, B.: Structural, lithological, and geodynamic controls on geothermal activity in the Menderes geothermal Province (Western

990   Anatolia, Turkey), Int. J. Earth Sci., 108, 301-328, https://doi.org/10.1007/s00531-018-16 2019

Saar, M. O., and Manga, M.: Depth dependence of permeability in the Oregon Cascades inferred from hydrogeologic, thermal, seismic, and magmatic modeling constraints, J. Geophys. Res., 109, B04204, https://doi.org/10.1029/2003JB002855 2004.

Scott, S., Driesner, T. and Weis, P.: Geologic controls on supercritical geothermal resources above magmatic intrusions. Nat Commun 6, 7837, https://doi.org/10.1038/ncomms8837 2015.

995 Scott, S., and Driesner, T.: Permeability changes resulting from quartz precipitation and dissolution around upper crustal intrusions, Geofluids, 2018, 6957306, 19 p. https://doi.org/10.1155/2018/6957306 2018.

Sibson, R.H.: Implications of fault-valve behaviour for rupture nucleation and recurrence, Tectonophysics, 211, 283-293, https://doi.org/10.1016/0040-1951(92)90065-E 1992.

Scibek, J.: Multidisciplinary database of permeability of fault zones and surrounding protolith rocks at world-wide sites, Sci.

1000   Data, 7, 95, https://doi.org/10.1038/s41597-020-0435-5 2020.

Simms, M. A., and Garven, G.: Thermal convection in faulted extensional sedimentary basins : theoretical results from finite-element modeling, Geofluids, 4, 109-130, https://doi.org/10.1111/j.1468-8115.2004.00069.x 2004.

Sonney, R., and Vuataz, F.-D.: Numerical modelling of Alpine deep flow systems: a management and prediction tool for an exploited geothermal reservoir (Lavey-les-Bains, Switzerland), Hydrogeol. J., 17, 601-616,

1005   https://doi.org/10.1007/s10040-008-0394-y 2009.

Stober, I., and Bucher, K.: Hydraulic conductivity of fractured upper crust: insights from hydraulic tests in boreholes and fluid-rock interaction in crystalline basement rocks, Geofluids, 15, 161-178, https://doi.org/10.1111/gfl.12104 2015.

Sutherland, R. et al., Extreme hydrothermal conditions at an active plate-bounding fault, Nature, 546, 137-151, https://doi.org/10.1038/nature22355 2017.

1010 Taillefer, A., Soliva, R., Guillou-Frottier, L., Le Goff, E., Martin, G., and Seranne, M.: Fault-related controls on upward hydrothermal flow: an integrated geological study of the Têt fault system, Eastern Pyrénées (France) Geofluids, 2017, 8190109, 19 p. https://doi.org/10.1155/2017/8190109 2017.

Taillefer, A., Guillou-Frottier, L., Soliva, R., Magri, F., Lopez, S., Courrioux, G., Millot, R., Ladouche, B., and Le Goff E.: Topographic and faults control of hydrothermal circulation along dormant faults in an orogen, Geochem. Geophys. Geosys,

1015   19, 4972-4995, https://doi.org/10.1029/2018GC007965 2018.

Tenthorey, E., and Cox, S.F.:Reaction-enhanced permeability during serpentinite dehydration, Geology, 31, 921-924, https://doi.org/10.1130/G19724.1 2003.

Tenthorey, E., and Fitz Gerald, J.D.: Feedbacks between deformation,hydrothermal reaction and permeability evolution in the crust: experimental insights, Earth Planet. Sci. Lett., 247, 117–129, https://doi.org/10.1016/j.epsl.2006.05.005 2006.

1020 Turcotte, D. L., and Schubert, G., Geodynamics, Second Edition, Cambridge University Press, 456 p., 2002

Violay, M., Heap, M.J., Acosta, M., and Madonna, C.: Porosity evolution at the brittle-ductile transition in the continental crust: Implications for deep hydrogeothermal circulation, Sci. Rep., 7, 7705, https://doi.org/10.1038/s41598-017-08108-5 2017.

Wang, M., Kassoy, D.R., and Weidman, P. D.: Onset of convection in a vertical slab of saturated porous media between two impermeable conducting blocks, Int. J. Heat Mass Transf., 30, 1331-1341, https://doi.org/10.1016/0017-9310(87)90165-7 1987.

Wanner, C., Diamond, L. W., and Alt-Epping, P.: Quantification of 3-D thermal anomalies from surface observations of an orogenic geothermal system (Grimsel Pass, Swiss Alps), J. Geophys. Res., 124, https://doi.org/10.1029/2019JB018335 2019.

Watanabe, N., Sakagushi, K., Goto, R., Miura T., Yamane, K., Ishibaashi, T., Chen, Y., Komai, T., and Tsuchiya, N.: Cloud-fracture networks as a means of accessing superhot geothermal energy, Sci. Rep.,9, 939, https://doi.org/10.1038/s41598-018-37634-z 2019.

Weis, P., Driesner, T., and Heinrich, C.A.: Porphyry-copper ore shells form at stable pressure-temperature fronts within dynamic fluid plumes, Science, 338, 1613-1616, https://doi.org/10.1126/science.1225009 2012.

Weis, P., Driesner, T., Coumou, D., and Geiger, S.: Hydrothermal, multiphase convection of H2O-NaCl fluids from ambient to magmatic temperatures: a new numerical scheme and benchmarks for code comparison, Geofluids, 14, 347-371, https://doi.org/10.1111/gfl.12080 2014.

Weis, P., The dynamic interplay between saline fluid flow and rock permeability in magmatic-hydrothermal systems, Geofluids, 15, 350-371, https://doi.org/10.1111/gfl.12100 2015.

Wüstefeld, P., Hilse, U., Lüders, V., Wemmer, K., Koehrer, B., and Hilgers, C.: Kilometer-scale fault-related thermal anomalies in tight gas sandstones, Mar. Petroleum Geol., 86, 288-303, https://doi.org/10.1016/j.marpetgeo.2017.05.015 2017.

Zhao, C., Hobbs, B. E., Mühlhaus, H. B., Ord, A., Lin, G.: Convective instability of 3-D fluid-saturated geological fault zones heated from below, Geophysical J. Int., 155, 213-220, https://doi.org/10.1046/j.1365-246X.2003.02032.x 2003.